tron contribution to the Coulomb and exchange potentials of the $5d$, $4f$, and other interior shells.

[14]A. J. Freeman, in Magnetism of the Rare Earth Metals, edited by R. J. Elliott (unpublished).

[15]C. Jackson, Phys. Rev. 178, 949 (1969).

[16]N. E. Christensen and B. O. Seraphin, Solid State Commun. 8, 1221 (1970); N. E. Christensen, Physics Laboratory I, Technical University of Denmark, Lyngby, Report No. 75, 1970 (unpublished).

[17]In Freeman's results (Ref. 14), for example, the d bandwidth is 0.35 Ry and ϵ_F lies 0.04 Ry above the d-band minimum, so that α is 0.11. Using this number together with our computed values ϵ (d top) $= +0.10$ Ry, ϵ (d bottom) $= -0.32$ Ry for Eu, we place ϵ_F at -0.27 Ry in our calculation through use of Eq. (4.1). α is in all cases roughly the fraction of $5d$ electrons present, which is consistent with the occupation of a d band having a constant density of states and a maximum occupancy of 10 electrons.

[18]E.g., L. Hedin and S. Lundqvist, *Solid State Physics*, Vol. 23, edited by D. Seitz, F. Turnbull, and H. Ehrenreich (Academic, New York, 1969), and references therein.

[19]A. P. Cracknell, Advan. Phys. 20, 1 (1971), and references therein.

PHYSICAL REVIEW B VOLUME 6, NUMBER 5 1 SEPTEMBER 1972

Brillouin Scattering from a Microwave-Phonon Bottleneck in MgO:Ni^{2+}

W. J. Brya,* S. Geschwind, and G. E. Devlin
Bell Laboratories, Murray Hill, New Jersey 07974
(Received 21 April 1972)

A large nonequilibrium distribution of microwave phonons arising from a phonon bottleneck has been observed in Ni-doped MgO using Brillouin light scattering; light scattering allows one to look *directly* at the phonons in a highly selective manner, and the intensity of the scattered light provides a direct measure of the effective temperatures of the phonons. With cw microwave saturation at 25.6 GHz of the $\Delta m_s = 1$ spin transitions of the Ni^{2+} ion ($S=1$) at an ambient temperature of 2 °K, the effective temperatures of slow-transverse acoustic phonons at 25.6 GHz propagating near a [110] crystal direction are increased to 270–4000 °K, while the bulk of the lattice modes remain at the ambient temperature; the observed phonon heatings are in reasonable agreement with theoretical predictions based on a simple rate-equation formalism applied to the $S=1$ system. The measured bandwidth for the heated phonons is ~180 MHz, which is significantly less than the spin resonance (EPR) linewidth of ~500 MHz but in qualitative agreement with theory. After switching off the saturating microwaves, the phonon heating decays away in a characteristic nonlinear manner; the initial rapid drop in phonon excitation indicates an effective phonon lifetime ~5 μsec which is not intrinsic but determined by crystal geometry and surface condition. In accord with this relatively long lifetime, the excess phonon heating is observed to persist to ambient temperatures as high as 40 °K. Under microwave saturation of the $\Delta m_s = 1$ transitions at frequency ν, significant heating of longitudinal phonons at ν and 2ν has also been observed. The heating of the "forbidden" longitudinal phonons at ν is ascribed to mode conversion of other heated ν phonons into the longitudinal phonons at crystal boundaries, while the 2ν phonon heating arises from $\Delta m_s = 2$ transitions in the $S=1$ spin system. In addition, anomalously large heating (up to 40 000 °K) of the slow-transverse phonons at ν has been observed in certain spatial regions of the crystals and is tentatively ascribed to a parametric process involving the 2ν phonons.

I. INTRODUCTION

In the usual description of the direct phonon process for spin-lattice relaxation, it is generally assumed that spins excited by resonant microwave radiation relax to phonons which are in such good contact with a thermal reservoir of infinite heat capacity (e.g., liquid helium) that the phonon excitation remains essentially at its thermal-equilibrium value. Van Vleck[1] pointed out many years ago, however, that the number of lattice modes on speaking terms with the spin system is actually quite limited. Consequently, if the spin-phonon coupling is strong and the thermalizing process for the phonons is slow, phonons generated over a frequency interval comparable to the EPR linewidth will be excited above their equilibrium value. This situation, now commonly known as a phonon bottleneck, modifies the observed spin-lattice relaxation time T_1 from that to be observed under the usual nonbottlenecked conditions and the relaxation is largely governed by the rate at which excess phonons can be dissipated.

Various experimental techniques have been employed to demonstrate the existence of the bottleneck. The usual spin-lattice relaxation-time measurements have disclosed unusual temperature dependences,[2] e.g., $T_1 \sim 1/T^2$ rather than $1/T$ as for the normal direct process, sample size and concentration dependences to T_1,[2,3] and nonexponential

recovery of the spin system.[4] Brya and Wagner[5] have given stronger evidence for the bottleneck by observing in an inverted spin system a decrease of several orders of magnitude in T_1 which was ascribed to a phonon avalanche; Mims and Taylor[6] have confirmed these results and obtained estimates for the effective phonon lifetime using spin-echo techniques. Shiren[7] also demonstrated the existence of the phonon avalanche and monitored the hot-phonon propagation down a crystal via a double-quantum detection method. Anderson and Sabisky[8] have shown evidence for the effect by saturating a spin system at one end of a crystal and using optical magnetic circular dichroism to detect an increase in spin temperature along the crystal length due to bottlenecked phonons; by using a sample doped with two paramagnetic species located in different spatial regions of the crystal, Rifman and Wagner[9] have also demonstrated the propagation properties of the hot phonons and obtained an estimate for the phonon bandwidth.

Essentially all of the above techniques, however, attempt to view the hot phonons indirectly by observing their averaged effect on a spin temperature. Consequently, only limited information about the detailed role of the phonons in the dynamics of the bottleneck is obtained. In contrast, the Brillouin–light-scattering technique allows one to look directly at the phonons in a highly selective manner. For a given choice of the scattering geometry one observes, from the totality of phonons, those propagating along a given direction in the crystal with a $\vec{k}$ vector determined by the scattering geometry. In addition, the intensity of the scattered light provides a direct measure of the effective temperature for the phonons and detailed studies of the phonon-system behavior under various excitations of the spin system are possible.[10]

In a previous paper[11] we presented our initial results on the observed phonon heating in the $MgO:Ni^{2+}$ paramagnetic system; since then, similar heating has been observed in the concentrated cerium-magnesium-nitrate salt[12] and for Nd^{3+} in $CaWO_4$.[13] In the present paper we describe the theoretical and experimental results on the $MgO:Ni^{2+}$ system in much greater detail. The simplified analysis of the bottleneck phenomenon for a two-level spin system is reviewed and the connection to our more complex $S=1$ case, whose analysis has been presented elsewhere,[14] is made; likewise, a brief sketch of the Brillouin-scattering formalism, as is directly applicable to our needs, is presented. The selection and orientation of the $MgO:Ni^{2+}$ samples, as well as the chosen experimental arrangement of this study, are governed by a variety of considerations which are discussed in Sec. IV. Experimental data on a number of different aspects of the bottleneck problem are presented and analyzed in Sec. V; these include the magnitude of the observed phonon heatings, the bandwidth of the heated phonons, relaxation profiles for the low-velocity transverse acoustic mode at a 2 °K bath temperature, the excess heating for this same phonon mode at elevated ambient temperatures to 40 °K, significant heating of "forbidden" longitudinal phonons at the resonant microwave frequency ascribed to phonon-mode conversion, heating of longitudinal phonons at twice the microwave frequency, and the anomalously large phonon heating of the low-velocity transverse mode in certain spatial regions of the samples. The Appendix details the spin-phonon-coupling selection rules applicable to the $MgO:Ni^{2+}$ system.

II. ANALYSIS OF BOTTLENECKED SPIN SYSTEM

Since most of the major physical features of the phonon bottleneck are common to both $S=\frac{1}{2}$ and $S=1$, we will use the simpler $S=\frac{1}{2}$ system as a framework for our discussion and draw upon Ref. 14 (hereafter referred to as DBSS) for those aspects of the bottleneck which are unique to the $S=1$ system.

The simplest model for the phonon bottleneck is based on rate equations for the spin populations and the resonant phonon excitation. Consider the doublet ground state of a paramagnetic species doped into an otherwise nonmagnetic host. The spin levels are separated by an energy $\hbar\omega_0$, with populations n_1 and n_2 in the lower and upper states, respectively. The excitation of the resonant phonons is described by the Bose factor for the occupation number per mode, i.e.,

$$p=(e^{\hbar\omega_0/kT_{eff}}-1)^{-1}, \tag{1}$$

where T_{eff} is an effective temperature for these phonons which may or may not be equal to the ambient (bath) temperature T.

In the usual manner, the rate equations for the level populations can be written[2,4]

$$\frac{d(n_2-n_1)}{dt}=-2K[(p+1)n_2-pn_1]-W_{rf}(n_2-n_1), \tag{2}$$

where K is the spontaneous emission rate for the direct (resonant) relaxation process and W_{rf} is the transition rate due to resonant microwave power. At low temperatures one can neglect the indirect (Raman and Orbach) relaxation processes which are, in general, unaffected by a bottleneck at energy $\hbar\omega_0$. Following the formalism of Faughnan and Strandberg,[4] we assume that the decay of the phonons in question may be described by a single phonon lifetime τ_{ph} in the absence of any interaction with the spin system. We may thus write

$$\frac{dp}{dt}=\frac{2K[(p+1)n_2-pn_1]}{2\rho(\nu_0)\,d\nu_0}-\frac{p-p^0}{\tau_{ph}}, \tag{3}$$

where $\rho(\nu_0)\,d\nu_0$ is the number of lattice modes in the frequency interval $d\nu_0$ which interact with the ions and the superscript denotes a thermal-equilibrium value. The first term on the right-hand side refers to phonon generation per mode by the spin system and the second describes the phonon decay. New variables are defined,

$$u=(n_2-n_1)/(n_1^0-n_2^0) \tag{4}$$

and

$$y=(p-p^0)/(p^0+\tfrac{1}{2})\ , \tag{5}$$

which represent normalized values for the population difference and the deviation of the phonon excitation from equilibrium. The rate equations then become

$$\frac{du}{dt}=-(u+1)\,T_{1D}^{-1}-uyT_{1D}^{-1}-W_{rf}u \tag{6}$$

and

$$\frac{dy}{dt}=[-y+\sigma(u+1)+\sigma uy]\tau_{\rm ph}^{-1}\ , \tag{7}$$

where the "bottleneck factor" is given by

$$\sigma=(n_1^0-n_2^0)\tau_{\rm ph}/(2p^0+1)\,T_{1D}\rho(\nu_0)\,d\nu_0 \tag{8}$$

and $T_{1D}^{-1}=K(2p^0+1)$ is the direct-process relaxation rate at the ambient temperature. σ is an important parameter in the theory and essentially describes the inability of the phonons in the limited bandwidth $d\nu_0$ to carry away the Zeeman energy to the bath rapidly enough to avoid heating of the phonon system. For a strongly bottlenecked system, $\sigma\gg1$.

If one subjects the spin system to steady-state complete cw saturation, such that $du/dt=dy/dt=0$ and $u\to0$ (with $-W_{rf}u\to1/T_{1D}$), one obtains from Eq. (7)

$$y_{\max}=(p-p^0)_{\max}/(p^0+\tfrac{1}{2})=\sigma\ . \tag{9}$$

Combining Eqs. (8) and (9), we find that, under complete saturation of the spin system, the excess phonon heating $(p-p^0)_{\max}$ produced by the relaxing spins is given by

$$(p-p^0)_{\max}=\frac{(n_1^0-n_2^0)\tau_{\rm ph}}{2T_{1D}\rho(\nu_0)\,d\nu_0}\ . \tag{10}$$

Less than complete saturation of the spins, i.e., $u\neq0$, will result in a lower value of p. As will be shown in Sec. III, *it is essentially the quantity p for selected phonons that is measured by Brillouin scattering*. Of course, Eq. (10) is the result of a simplified theory which assumes a uniform relaxation of the spins to all phonons at ν_0 as expressed by T_{1D}. In point of fact the spins will couple differently to phonons at the same ν_0 but traveling in different directions and with different polarizations. In a similar vein, $\tau_{\rm ph}$ is an average quantity for the phonons. Equation (10), however, is a reasonable point of departure in estimating the bottleneck while the selective heating of different phonons at the same ν_0 will be discussed and illustrated below.

By expressing p and p^0 in terms of their respective temperatures, one obtains the effective temperature for the resonant phonons for $u=0$,

$$T_{\rm eff}\sim(\sigma+1)T\ , \tag{11}$$

for $kT_{\rm eff}\geq kT\gg\hbar\omega_0$. Thus, even when $u=0$, corresponding to infinite spin temperature, $T_{\rm eff}$ does not rise above the value given by Eq. (11). Since $T_{1D}\propto v^5$ (where v is the velocity of sound) and $\rho(\nu_0)\propto1/v^3$, then $\sigma\propto1/v^2$ and one expects the heating to be greatest for the lowest-velocity acoustic modes; in addition, the heating expressed by Eq. (10) will be enhanced at the higher Zeeman frequencies, going as ν^3 for Kramers doublets and as ν for non-Kramers systems.

One can obtain an estimate of the hot-phonon bandwidth based on our previous discussions. For an inhomogeneously broadened spin-resonance line of width $d\nu_s$, each of the constituent homogeneous spin packets has its characteristic bottleneck factor σ_i, which differs from the others through the population differential $(n_1^0-n_2^0)_i$. Since the phonon heating is proportional to σ_i, and hence to $(n_1^0-n_2^0)_i$, saturation of the complete inhomogeneous line is expected to produce a phonon bandwidth $d\nu_0\approx d\nu_s$. This latter point will be returned to later.

When the resonant microwaves are removed, the saturated spin system and the heated phonons will relax to their equilibrium values in accordance with the rate equations. Because the equations are nonlinear, they do not appear to be soluble except by numerical techniques. Near the end of the decay, however, where $u\to-1$ and $y\to0$, Eqs. (6) and (7) can be linearized to yield two decay times, the longer of which is[2]

$$T_1^{\rm obs}=(\sigma+1)T_{1D}\ . \tag{12}$$

This asymptotic time constant characterizes the final return of the spin and phonon systems to equilibrium and is the quantity obtained in previous pulse-saturation spin-lattice-relaxation studies. By referring to the expression for σ given by Eq. (8), we see the modifications which are produced in the observed T_1 due to the bottleneck and which were referred to in the Introduction. For example, since $(2p^0+1)\sim\coth(\hbar\omega_0/2kT)$, $(n_1^0-n_2^0)\sim\tanh(\hbar\omega_0/2kT)$, and $T_{1D}\sim\tanh(\hbar\omega_0/2kT)$, then $\sigma\sim\tanh(\hbar\omega_0/2kT)$ or $\sigma\sim1/T$ for $\hbar\omega_0\ll kT$. Thus for $\sigma>1$ and $\hbar\omega_0\ll kT$, $T_1^{\rm obs}\sim(1/T^2)$. In addition, we see from Eqs. (8) and (12) that $T_1^{\rm obs}$ will be proportional to impurity concentration via $(n_1^0-n_2^0)$

and proportional to sample size to the extent that τ_{ph} is determined by sample dimensions. It will be seen later that at low temperatures τ_{ph} is essentially the escape time of the phonons from the crystal.

As pointed out in DBSS[14] and as will be seen in Sec. V C, an experimental determination of T_1^{obs} from the phonon relaxation is hindered by the low phonon excitations at long times; this decay time is more easily obtained from the usual spin-lattice-relaxation measurements. Rather, the phonon decays are of more interest just after removal of the saturating microwaves. In Fig. 1 are shown typical phonon-decay profiles at early times, obtained from numerical solutions to Eqs. (6) and (7), under the condition of complete initial saturation of the spin system. The decays begin with zero slope, quickly speed up for a short time, and then slowly return to equilibrium over a much longer time; the initial zero slope of the decay is a result of the fact that the phonons are being generated by relaxing spins and, following the switching off of the microwaves, their excitation cannot change until the spin-system heating has decreased. Variations in the system parameters modify the actual decay curves; for example, the larger σ, the steeper and more pronounced will be the region of fast decay. In addition, for larger σ, the region of much slower decay time which follows corresponds to a lower value of fractional excitation referred to the initial value, as illustrated in Fig. 1. While the region of fast decay may obviously never exceed τ_{ph}, an analysis of the phonon-decay profiles shows that, when $(\sigma\tau_{ph}/T_{1D}) \gg 1$, the initial rapid decay of the phonon excitation proceeds in exponential fashion over at least half a decade with a time constant which approaches τ_{ph}. Thus, for those cases where $(\sigma\tau_{ph}/T_{1D}) \gg 1$, a direct determination of τ_{ph} should be possible. This feature as well as the general nonlinear recovery of the phonon system as seen by Brillouin scattering will be emphasized in Sec. V C.

In general, the preceding results for the two-level spin system carry over essentially unchanged into the more complex three-level $S=1$ spin system as detailed in DBSS.[14] For the three-level case, one now has as many as three separate spin-transition frequencies ($\Delta m_s = \pm 1, \pm 2$) with their associated bottlenecked resonant phonons. Under a condition of cw saturation, these phonons attain effective temperatures T_{eff} similar to that given by Eq. (11) with appropriately defined bottleneck factors σ. The asymptotic relaxation time T_1^{obs} is considerably more complex; however, the rapid initial decays in the various phonon decays still provide determinations of the effective phonon times τ_{ph} in a strongly bottlenecked material.

The most significant differences between the two- and three-level systems occur for the hot-phonon bandwidths. With cw saturation of the inhomogeneously broadened $\Delta m_s = \pm 1$ resonance line, the bandwidth of phonons produced by $\Delta m_s = \pm 1$ spin transitions will be noticeably less than the EPR bandwidth for $S=1$; this occurs because the exchange of spin and phonon energy at the center of the resonance, where the spin levels are equally spaced, produces more phonons than is possible out in the wings of the EPR line. For those phonons generated by the $\Delta m_s = \pm 2$ spin transitions, the situation is further changed. With saturation of the $\Delta m_s = 1$ transitions at energy δ, phonon heating at 2δ is now very intense at line center where strong double-quantum transitions can saturate all the spin packets and where the energy exchange

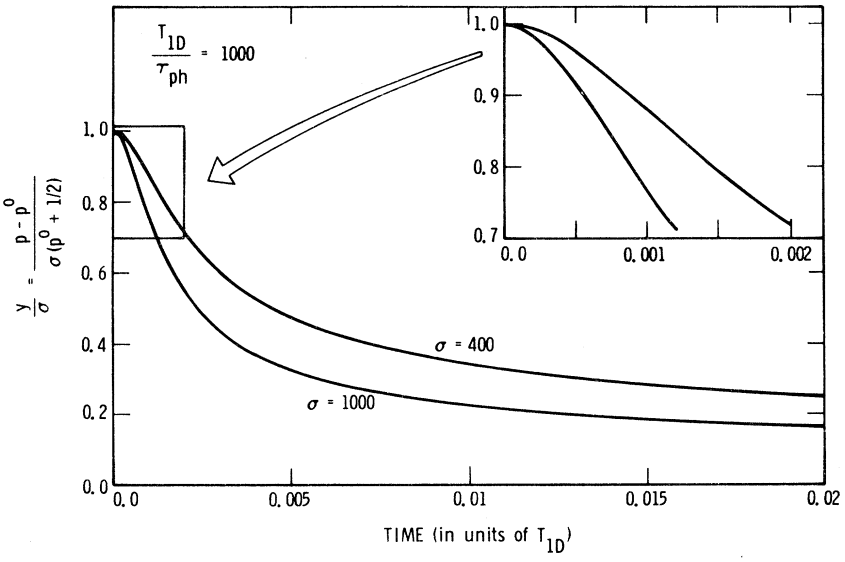

FIG. 1. Normalized characteristic phonon-relaxation curves obtained from numerical solutions to the rate equations, Eqs. (6) and (7); the saturating rf field is switched off at $t=0$. The inset expands the region near $t=0$ and shows the initial zero slopes of the decays. Spin excitations show negligible change over the given time interval. Note that for larger σ the decay is steeper and drops to a smaller fraction of the initial excitation.

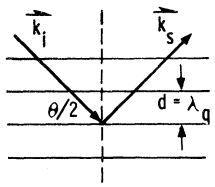

1. $2d \sin\frac{\theta}{2} = \lambda_i/n$

2. $\nu_s - \nu_i = \frac{2\nu_i v \sin\frac{\theta}{2}}{c/n}$

$\therefore \nu_s - \nu_i = \frac{v}{\lambda_q} = \nu_q$

(a)

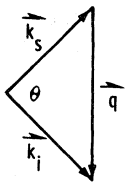

3. $\vec{k}_i = \vec{k}_s + \vec{q}$

4. $\hbar\omega_i = \hbar\omega_s \pm \hbar\omega_q$

(b)

FIG. 2. Classical and quantum-mechanical formalisms for Brillouin light scattering from acoustic phonons. (a) Classical formalism views light scattering as a Bragg reflection of light from a moving grating with spacing equal to the phonon wavelength. Equation (1) is the Bragg reflection criterion; Eq. (2) is the Doppler shift of the incident light due to the moving grating. All notation is explained in the text. (b) Quantum-mechanical formalism utilizes the conservation-of-momentum diagram shown to describe the inelastic-scattering event. The kinematics of the event require the conservation of wave vector or quasimomentum [Eq. (3)] and of energy [Eq. (4)].

between spin levels is relatively easy. As a result, the 2δ phonon bandwidth should be significantly less than either the EPR or δ phonon linewidths.

III. BRILLOUIN-SCATTERING FORMALISM

The acoustic waves which propagate in a liquid or solid produce periodic spatial fluctuations in the dielectric constant of the medium. Brillouin scattering[15] is the inelastic scattering of a beam of light from these fluctuations. As shown in Fig. 2(a), the scattering process can be viewed as a Bragg reflection of light from a dielectric grating with a spacing equal to the acoustic wavelength; the light scattered at an angle θ from the incident direction is related to the acoustic wavelength λ_q by the Bragg condition

$$\lambda_i/n = 2\lambda_q \sin\tfrac{1}{2}\theta \ , \tag{13}$$

where λ_i/n is the wavelength of the incident light in a medium with index of refraction n. The grating, however, is traveling with the velocity of sound $\pm v(q)$ and the scattered light suffers a Doppler shift to the frequencies $\nu_i \pm \Delta\nu_i$ with

$$\Delta\nu_i = 2(nv/c)\nu_i \sin\tfrac{1}{2}\theta \ , \tag{14}$$

where ν_i is the frequency of the incident light and c is the velocity of light in vacuum. Combining Eqs. (13) and (14), one obtains

$$\Delta\nu_i = v/\lambda_q = \nu_q \ , \tag{15}$$

with ν_q the frequency of the acoustic wave. Thus, the scattered light is shifted to lower and higher frequencies by an amount equal to the acoustic wave frequency.

In a quantum-mechanical formalism, Brillouin scattering is regarded as an inelastic-scattering event in which an incident photon of wave vector $\vec{k}_i$ and frequency ν_i is scattered into a photon of wave vector $\vec{k}_s$ and frequency ν_s with the emission or absorption of a phonon of wave vector $\vec{q}$ and frequency ν_q, as depicted in Fig. 2(b). The kinematics of the event require the conservation of energy

$$\hbar\omega_i = \hbar\omega_s \pm \hbar\omega_q \tag{16a}$$

and the conservation of wave vector or quasimomentum

$$\vec{k}_i = \vec{k}_s \pm \vec{q} \ , \tag{16b}$$

where the plus sign corresponds to emission of a phonon and the minus sign to absorption. One notes that the maximum of $|\vec{q}|$ is of the order of $|\vec{k}_i|$. Since the phonon velocity is very much less than the velocity of light, then $\omega_q \ll \omega_i$, ω_s. Thus, $\omega_i \simeq \omega_s$ and $|\vec{k}_i| \simeq |\vec{k}_s|$. As a result, $|\vec{q}| = 2|\vec{k}_i| \times \sin\frac{1}{2}\theta$ and one obtains

$$\nu_q = 2(nv/c)\nu_i \sin\tfrac{1}{2}\theta \ , \tag{17}$$

which is the same as Eqs. (14) and (15).

In a solid there are three branches to the acoustic spectrum corresponding to the two primarily transverse phonon modes and the primarily longitudinal phonon mode. In general, each of these has a different sound velocity and, as is seen from Eq. (14), each will produce scattered light with a different frequency shift for a fixed scattering angle. One also notes from Eq. (14) that, as the scattering angle is varied from $\theta = 0$ in the forward direction, the phonon frequency probed increases from zero to a maximum value for backscattering of $\nu_q(\max) = 2(nv/c)\nu_i$. For solids, where $v/c \approx 10^{-5}$, $\nu_q(\max)$ is of the order of 10–50 GHz and Brillouin scattering is eminently suited to probing the properties of phonons in the microwave-frequency regime.

Benedek and Fritsch[15] have presented a classical calculation of the intensity, polarization, and spectral distribution of the scattered light in solids along with the quantum-mechanical modifications necessary for its application at low temperatures. They show that for $\hbar\omega_q \ll kT$ the intensity I of light in all frequencies scattered into a solid angle $d\Omega$ is given by

$$I \propto E_i^2 \nu_i^4 \epsilon_0^4 T \sum_{\mu=1}^{3} \frac{|\vec{\xi}_\mu|^2}{v_\mu^2(\vec{q})} d\Omega \ , \tag{18}$$

where E_i is the incident electric field intensity, ϵ_0 is the optical dielectric constant, and T is the temperature. The index μ denotes the three acoustical branches of the phonon spectrum, and $v_\mu(\vec{q})$ is the sound velocity of mode μ with wave vector $\vec{q}$. The quantity $\vec{\xi}_\mu$ is a vector of magnitude $0 < |\vec{\xi}_\mu| \lesssim 1$ and the $|\vec{\xi}_\mu|^2$ serve as weighting factors which determine the relative scattering intensities for the three Brillouin doublets. $\vec{\xi}_\mu$ is given by

$$\vec{\xi}_\mu = \vec{1}_{k_s} \times (\vec{1}_{k_s} \times \vec{\xi}_\mu) \ , \tag{19a}$$

where, for a cubic system,[16]

$$\vec{\xi}_\mu = p_{44}[\vec{\pi}_\mu(\vec{1}_q \cdot \vec{1}_{E_i}) + (\vec{\pi}_\mu \cdot \vec{1}_{E_i})\vec{1}_q] + p_{12}(\vec{\pi}_\mu \cdot \vec{1}_q)\vec{1}_{E_i}$$
$$+ (p_{11} - p_{12} - 2p_{44}) \sum_{m=1}^{3} (\vec{\pi}_\mu)_m (\vec{1}_q)_m (\vec{1}_{E_i})_m \vec{1}_m \ . \tag{19b}$$

$\vec{1}_{k_s}$ is a unit vector in the direction of propagation of the scattered light $\vec{k}_s$. The p_{ij} are the Pockels elasto-optic constants for the cubic system. $\vec{\pi}_\mu$ is a unit vector in the direction of polarization of the sound wave with the components $(\vec{\pi}_\mu)_m$ along the cube axes, $m = 1, 2, 3$. $\vec{1}_q$ is a unit vector in the direction of propagation of the sound wave with components $(\vec{1}_q)_m$, and $\vec{1}_{E_i}$ is a unit vector along the direction of polarization of the incident field with components $(\vec{1}_{E_i})_m$. The $\vec{1}_m$ are unit vectors along the cube axes. Thus the magnitudes of the scattering intensities for the phonon modes are determined by the relative directions of $\vec{q}$, $\vec{E}_i$, and $\vec{\pi}_\mu$ and the magnitudes of the p_{ij}.

Equation (18) was obtained under the assumption $\hbar\omega_q \ll kT$ and predicts that the intensities of the light shifted to lower (Stokes) and higher (anti-Stokes) frequencies by a given phonon mode are equal and proportional to the temperature. At very low temperatures, however, this result must be altered to take into account the quantum-mechanical features of the phonons, i.e., the spontaneous emission of a phonon in the scattering process. When this is properly done, one finds that the intensities of the Stokes and anti-Stokes lines are proportional to $p_\mu(\vec{q}) + 1$ and $p_\mu(\vec{q})$, respectively, where $p_\mu(\vec{q})$ is the excitation number of phonons in mode μ with wave vector $\vec{q}$ and frequency $\omega(\vec{q})$; $p(\vec{q})$ is given by Eq. (1). Thus at low temperatures the intensity of the Stokes line becomes temperature independent while the anti-Stokes intensity drops off more rapidly with temperature than T, as given in Eq. (18). In practice, one can use the measured scattered intensity to obtain the phonon excitation number $p_\mu(\vec{q})$ and thereby assign an effective temperature to a phonon mode.

IV. EXPERIMENTAL PROCEDURE

A. Selection and Orientation of Paramagnetic Sample

The selection of nickel-doped magnesium oxide as the system of study was based on several factors. Previous microwave spin-lattice-relaxation measurements and phonon-avalanche studies have shown that the MgO:Ni^{2+} system does exhibit phonon bottleneck behavior at liquid-helium temperatures.[7] Also the elastic[17] and elasto-optic[18] properties of MgO are well documented; thus the frequency shifts and scattering intensities for the various acoustical modes so necessary to the Brillouin scattering can be determined with reasonable accuracy. Finally, the physical properties of MgO permit the precise fabrication of samples of high optical quality which can be specifically oriented to observe the Brillouin scattering from selected acoustic modes strongly coupled to the Ni^{2+} ions.

The solution of the secular equation[19] for the propagation of elastic waves in a solid provides the velocities of sound and polarizations for the three acoustic waves. As indicated in Sec. II, one expects the bottleneck to be strongest for the lowest-velocity mode, other factors being equal. Calculations for cubic MgO in (100), (110), and (111) crystal planes show that the lowest-velocity mode is a nondegenerate transverse wave propagating along a [110] direction with a velocity of 5.30×10^5 cm/sec at room temperature. With incident light of 5145-Å wavelength (chosen to coincide with a minimum in the optical-absorption spectrum[20] of MgO:Ni^{2+}) and refractive index $n = 1.743$,[21] Eq. (14) yields a Brillouin frequency shift of 25.4 GHz for this mode with the convenient 90° scattering geometry. This relatively high frequency enhances the bottleneck as predicted by Eq. (10), yet is low enough to ensure microwave klystron output powers sufficient to produce saturation of the spin system.

Using a fixed 90° scattering geometry and variable incident-light polarization, Eq. (18) was then solved for the Brillouin-scattered light intensity arising from acoustic modes propagating in (100), (110), and (111) planes. This analysis was adopted to determine that scattering configuration which maximizes the scattered intensity for a low-velocity [110] transverse mode; hopefully this maximum occurs with the incident light polarized in the scattering plane, thereby minimizing any elastic Rayleigh and/or Tyndall scattering present. Our results show that the scattering from this mode (with the incident light polarized in the scattering plane) is relatively large for a (110) plane. Scattering in a (111) plane for this same mode is noticeably less, while it is strictly forbidden by symmetry considerations in a (100) plane.

The coupling of the Ni^{2+} spin system ($S = 1$) to acoustic waves propagating in a (110) plane is eas-

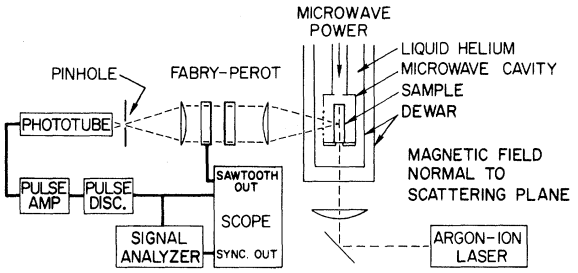

FIG. 3. Experimental Brillouin–light-scattering arrangement showing the laser, light-focusing and collection systems, sample and microwave cavity assembly, scanning Fabry-Perot interferometer, and photoelectric detection system. The interferometer sweep and signal analyzer trigger are derived from the time base of the oscilloscope.

ily determined using the spin-lattice interaction formalism detailed in the Appendix. For a static Zeeman field directed normal to a (110) scattering plane, the resultant selection rules for the single-phonon interaction are rather restrictive: $\Delta m_s = \pm 1$ transitions couple only to pure transverse waves polarized normal to the scattering plane (i.e., the slow-transverse mode in this case); longitudinal and transverse waves polarized in the scattering plane are connected only to $\Delta m_s = \pm 2$ transitions. The applied microwaves pump the $\Delta m_s = \pm 1$ transitions (aside from double-quantum absorptions) and one therefore anticipates a stronger bottleneck for those low-velocity modes directly coupled to these same transitions. In addition, the anisotropy in the spin-lattice coupling for phonons traveling in the (110) plane arises primarily from the anisotropy in the velocity of sound. This fact further suggests that the bottleneck will be strongest for the lowest-velocity modes.

B. Brillouin-Scattering Arrangement

A schematic diagram of the basic experimental apparatus is given in Fig. 3. A $3\times3\times6$-mm^3 sample of MgO: Ni^{2+} is mounted in a cylindrical microwave cavity which is resonant at 25.6 GHz in the TE_{011} mode when immersed in liquid He. While the majority of measurements are made at a temperature of 2 °K in the liquid, data are also collected over an elevated temperature range with a cryogenic system which utilizes a flow of cold He gas as described elsewhere.[22] A static Zeeman field is applied along a $[1\bar{1}0]$ crystal direction to tune the ground-state $\Delta m_s = \pm 1$ paramagnetic transitions of the Ni^{2+} ion to the cavity resonance. Continuous saturation of these transitions is produced by an 800-mW reflex klystron.

An argon-ion laser, which operates continuously in a single-longitudinal-mode single-frequency configuration, delivers 250 mW at 5145 Å with a typical frequency stability of ± 50 MHz. The focused laser output passes through the glass Dewar bottom, enters through a hole in the bottom of the cavity, and traverses the sample; a high-reflectivity dielectric mirror deposited on the exit face of the sample returns the beam along its original path and out the cavity bottom. It was necessary to return the incident laser beam back out of the cavity with this mirror in order to minimize stray unshifted laser light. In addition, the return beam allowed us to view simultaneously another phonon as will be described below. Light scattered at right angles to the laser beams is observed through a series of fine slits cut in the side wall of the microwave cavity. The scattered light is collected with an $f/6.7$ optical system, frequency analyzed with a piezoelectrically scanned Fabry-Perot interferometer,[23] and detected with a cooled ITT FW-130 photomultiplier. The phototube output is then processed using conventional pulse-counting circuitry and presented either to an oscilloscope for direct viewing or to a multichannel analyzer for signal averaging.

The $f/6.7$ optical collection system was adopted in order to accept a range of Brillouin-scattering frequencies larger than the measured EPR linewidth (~ 500 MHz for the applied $[1\bar{1}0]$ Zeeman field of 8300 G) of the $\Delta m_s = \pm 1$ spin transitions of the Ni^{2+} ions at 2 °K. The Fabry-Perot apparatus utilized optical plates of $\frac{1}{200}\lambda$ flatness (claimed) coated for 97–98% reflectivity at 5000 Å, a plate spacing $\simeq 3$mm, an $f/11$ exit lens, and 1.25-mm-diam pinhole; a bandpass filter centered at 5145 Å was interposed between the final pinhole and the phototube to reject unwanted laser discharge lines and objectionable sample fluorescence.

The basic scattering geometry for the oriented sample is illustrated in Fig. 4(a). The incident and reflected laser beams $\vec{k}_i$ are directed along the longest sample dimension, while the 90° scattered radiation $\vec{k}_s$ is observed along the [111] direction; the scattering plane determined by $\vec{k}_i$ and $\vec{k}_s$ is the $(1\bar{1}0)$ crystal plane. As seen in Fig. 4(b) the incident beam is scattered from those modes with wave vector $\vec{q}_A$, which lie near the [110] direction (ease of sample orientation dictated the accepted scattering geometry which places $\vec{q}_A$ 10° off the optimum [110] direction; the resulting 1% increase in sound velocity for the low-velocity mode is inconsequential). For the reflected beam [see Fig. 4(c)], however, scattering arises from modes propagating along $\vec{q}_B$, which is near the [001] direction. Because these directions are crystallographically inequivalent, the velocity of sound for modes from the same acoustic branch propagating along $\vec{q}_A$ and $\vec{q}_B$ will generally be different; therefore, their Brillouin shifts will also differ. For the transverse acoustic branch of interest to this

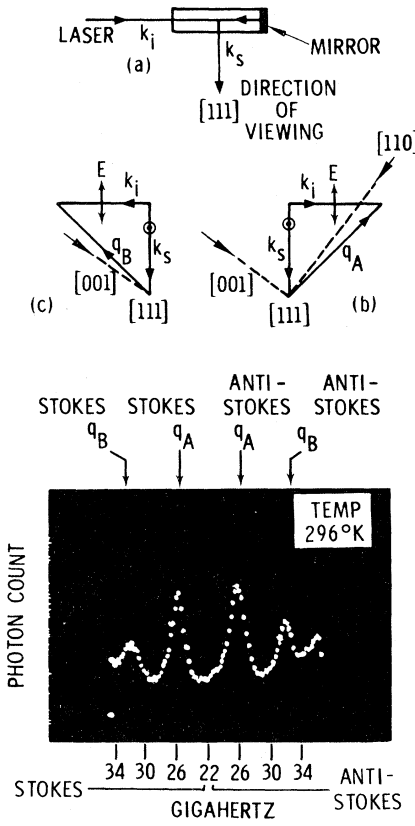

FIG. 4. 90° Brillouin–light-scattering arrangement for MgO:Ni^{2+} crystals. (a) Incident and reflected laser beams are directed along $\pm\vec{k}_i$; the scattered light $\vec{k}_s$ is viewed along the [111] crystal direction. The scattering plane is the $(1\bar{1}0)$ crystal plane. (b) Scattering diagram for incident beam with polarization $\vec{E}$ in the scattering plane; scattered beam polarized normal to scattering plane. Scattering arises from acoustic phonons with wave vector $\pm\vec{q}_A$; dashed lines denote principal axes of the crystal. (c) Scattering diagram for the reflected laser beam; scattering arises from acoustic modes of wave vector $\pm q_B$. Photograph: Room-temperature (296 °K) Brillouin scattering from low-velocity transverse acoustic phonons of wave vector $\vec{q}_A$ and $\vec{q}_B$ in MgO:Ni^{2+}. Abscissa denotes frequency shift of the Stokes and anti-Stokes lines from the laser frequency. Elastic scattering occurs at zero-frequency shift and is not shown.

study, $\nu(\vec{q}_A) = 25.6$ GHz and $\nu(\vec{q}_B) = 31.3$ GHz at 2 °K. The phonons $\nu(\vec{q}_B)$ are used to monitor the crystal temperature and to show that the bottleneck, which is produced by the relaxing spin system, is selective at 25.6 GHz, the resonant frequency of the saturated Ni^{2+} spins in the external Zeeman field.

Figure 4(d) shows a typical Brillouin-scattering spectrum for MgO obtained at room temperature for the configuration described above. The scattered light is shifted to lower (Stokes) and higher (anti-Stokes) frequencies relative to the laser frequency corresponding to the creation and destruction of phonons, respectively. We show here only the scattering from the pure transverse modes in the directions $\vec{q}_A$ and $\vec{q}_B$. The free spectral range of the Fabry-Perot interferometer has been adjusted to show the Stokes and anti-Stokes lines from adjacent interference orders. The scattering from the longitudinal modes (which occur at frequencies of ~45 GHz) lies in the region of the elastic Rayleigh/Tyndall scattering peak and is not shown; scattering from the "fast"-transverse modes at ~31 GHz is not observed since their intensities are about two orders of magnitude weaker than those of the "slow"-transverse modes due to the chosen scattering geometry. As detailed in Eq. (18), the observed scattering intensities for the slow-transverse modes are determined by several factors; most important to this study, however, is that these intensities are direct measures of the effective temperatures of the acoustic modes.

V. EXPERIMENTAL RESULTS

A. Brillouin Scattering from Slow-Transverse Phonons at 2 °K

Thermal Brillouin scattering at liquid-helium temperatures is more than two orders of magnitude weaker than the room-temperature intensity. In order to observe the thermal Brillouin scattering at 2 °K, the free spectral range of the Fabry-Perot was therefore adjusted so that the Stokes and anti-Stokes lines from phonons $\vec{q}_A$ at 25.6 GHz, which are shown separated in Fig. 4(d), are now made to overlap, as shown in Fig. 5, to improve the S/N. In Fig. 5(β) is shown the thermal Brillouin scattering at 2 °K. When $\Delta m_s = 1$ transitions of the Ni^{2+} spin system are saturated with microwaves at 25.6 GHz, however, the scattering intensity is drastically modified. Figure 5(α) shows a factor-of-30 increase in peak scattering intensity from the $\nu(\vec{q}_A)$ phonons for sample (MS-2C), of ~1% Ni^2 concentration, undergoing microwave saturation. By contrast, the phonons $\nu(\vec{q}_B)$ at 31 GHz remain at the 2 °K bath temperature and are not being heated by the relaxing spins at 25.6 GHz, as expected. Indeed it will be shown in Sec. V B that the bandwidth of the heated phonons at $\nu(\vec{q}_A)$ is within the EPR linewidth.

An estimate of the effective temperature of the heated phonons cannot be made by simply comparing the peak intensities of the α and β curves in Fig. 5; account must be taken of the different bandwidths of the thermal phonons in Fig. 5(β) and of the heated phonons in Fig. 5(α), each of which in turn is less than the instrumental width. As will be seen in Sec. V B, the actual hot-phonon bandwidth for this sample is ~200 MHz, which is significantly less than the bandpass of either the input

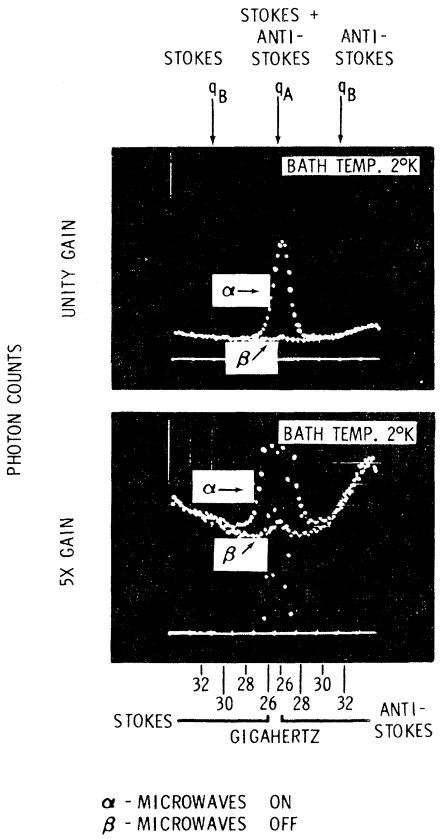

FIG. 5. Brillouin scattering from low-velocity transverse acoustic phonons in MgO:Ni^{2+} at a bath temperature of 2 °K. A magnetic field of 8300 G is applied normal to the $(1\bar{1}0)$ scattering plane. Integration time is 3 min. In order to improve the signal-to-noise ratio, the interferometer spacing has been adjusted so that Stokes and anti-Stokes lines, from adjacent orders, for $\nu(\vec{q}_A)$ shown in Fig. 4 are made to overlap. (α) Microwave saturation of the Ni^{2+} ground-state spin levels at 25.6 GHz, showing a factor-of-30 increase in peak scattering compared to (β). (β) No microwaves, i.e., thermal scattering at 2 °K.

collection lens or the Fabry-Perot interferometer. The bandwidth of the observed thermal phonons, however, is determined primarily by the input collection lens. With the Fabry-Perot bandpass (≥ 1.2 GHz) greater than either of these bandwidths, one therefore expects the peak scattering intensity of the heated phonons to appear reduced relative to the thermal-phonon intensity by the ratio of the thermal-phonon bandwidth to the hot-phonon bandwidth. For the low-velocity transverse phonons which we observe, the $f/6.7$ collection lens gathers thermal phonons over a range of ~1.1 GHz. When this figure is combined with the Fabry-Perot bandpass, we estimate an effective thermal-phonon bandwidth of ~900 MHz. This ratio of 4.5 in bandwidths, multiplied by the factor-of-30 increase in peak scattering intensity, yields a factor-of-135 increase in phonon excitation or an effective hot-phonon temperature of ~270 °K at the ambient 2 °K.

The phonon heating of 270 °K occurs with the microwave frequency tuned off the center of the Ni^{2+} resonance line; slight changes in the applied magnetic field and/or the microwave frequency have little effect on the heating. With optimization of the magnetic field and the microwave frequency, one can saturate the center of the Ni^{2+} resonance and the hot-phonon temperature then increases to ~540 °K for this same sample. The heating, however, is now a sensitive function of the applied field and frequency and small changes in either cause the phonon temperature to drop quickly to the 270 °K value. In all instances, the $\nu(\vec{q}_B)$ phonons do not depart from their 2 °K equilibrium value.

Another sample (MS-4A) of similar size and orientation was fabricated from different material of almost identical measured Ni^{2+} concentration. On saturating the center of the Ni^{2+} resonance with microwaves at 25.6 GHz, the resonant phonons $\nu(\vec{q}_A)$ are heated in this sample to a corrected temperature ~4000 °K. Off line center the heating drops to ~1600 °K. Once again no heating of the $\nu(\vec{q}_B)$ phonons was detected. The larger value of phonon heating observed in sample 4A is ascribed to a longer τ_{ph} in this sample as will be argued below.

We now compare the experimentally observed phonon heating with values predicted from the bottleneck theory. A reasonable estimate of the anticipated heating for the slow-transverse (ST) mode is obtained from a generalized expression for Eq. (11) applicable to the $S=1$ spin system. As shown in Eqs. (2) and (5) of DBSS,[14] the phonon heating under saturation of the Ni^{2+} resonance at line center is obtained from Eq. (11), where the bottleneck factor σ is given by the relation

$$\sigma = 2NK_1\tau_{ph}/3(p^0+\tfrac{1}{2})\rho(\nu_0)\,d\nu_0 \ . \qquad (20)$$

Here N is the total number of spins at line center and p^0 is the equilibrium excitation of the resonant phonons; $\rho(\nu_0)\,d\nu_0$ is the number of resonant ST lattice modes in the frequency interval $d\nu_0$ which interact with the ions. τ_{ph} is the effective phonon lifetime for the ST modes at the ambient temperature and K_1 is the spontaneous emission rate for direct spin relaxation due solely to the ST phonons. K_1 is obtained from the expression

$$K_1 = \pi\nu_0\rho(\nu_0)G^2/\hbar M v^2 \ , \qquad (21)$$

where M is the crystal mass and v is the velocity of sound of the ST mode. G is a spin-phonon-coupling constant which, in general, is a function of the applied magnetic field orientation and the propagation direction and polzarization of the phonon;

this functional dependence is easily determined using the spin-lattice interaction formalism described in the Appendix. Since one is interested of course in the rate at which the spins are exciting that particular class of phonons under observation, one must use a G appropriate to the ST phonons traveling close to the [110] direction. The value of $G \simeq 57$ cm^{-1} is taken from the strain data on Ni^{2+} in MgO of Shiren[24] and Watkins and Feher.[25] K_1, thus determined, corresponds to an effective feeding rate per spin, for these particular phonons, given by

$$1/(T_{1D}^{\text{eff}}) = K_1(p^0 + \tfrac{1}{2}) \ . \tag{22}$$

This value of T_{1D}^{eff} is the appropriate one to use in discussing the heating of these particular phonons in terms of the bottleneck factor σ, as given by Eq. (8), for example, where T_{1D} appears explicitly. The use of an experimentally measured unbottlenecked T_{1D} to estimate σ assumes equal and isotropic heating of all the resonant phonons and is not appropriate to our case where the phonons are selectively heated as will be seen below. The value of T_{1D}^{eff} using $G \simeq 57$ cm^{-1} is found to be 10^{-3} sec, which is within the range of the actual T_1 extrapolated to 25.6 GHz from the work[26] of Lewis and Stoneham at 9.3 GHz.

The anticipated phonon heating is estimated using the following values of the additional parameters: $T = 2\,^\circ$K, $\nu_0 = 25.6$ GHz, $v = 5.34 \times 10^5$ cm/sec. The phonon lifetimes, $\tau_{ph} \simeq 5.4$ μsec for sample MS-4A and 0.8 μsec for MS-2C, are taken from results to be presented in a later section. For the ratio $N/d\nu_0$ we assume complete saturation so that all of the Ni^{2+} ions in an MgO:Ni^{2+} sample of 1% concentration are active in producing phonons over the observed hot-phonon bandwidth of 200 MHz, which is less than the 520-MHz EPR bandwidth.

With this choice of parameters, one obtains $T_{\text{eff}} \sim 4200\,^\circ$K for $\tau_{ph} \sim 5.4$ μsec, as compared to the observed $T_{\text{eff}} \sim 4000\,^\circ$K obtained for sample MS-4A at line center. Similarly, for $\tau_{ph} \sim 0.8$ μsec we estimate $T_{\text{eff}} \sim 600\,^\circ$K compared to the observed value of $540\,^\circ$K. Considering the number of different factors involved in the comparison, the agreement is fortuitously good. For example, our estimate of the Ni^{2+} concentration in the sample is only good to within a factor of 2 and similarly for τ_{ph}. In addition, if one fails to saturate all the spin packets in the full inhomogeneous linewidth, then a smaller value of N should be used in association with the observed hot-phonon bandwidth in estimating σ in Eq. (20). We believe that both spin diffusion, for this relatively concentrated sample, and the effectiveness of the two-quantum absorption at high-power levels bring about complete saturation of the EPR line. This is difficult to ascertain with certainty, however, because of the strong dispersive properties of the sample.

B. Measurement of Bandwidth of Hot Phonons

Given the finesse of 50 of the Fabry-Perot and the free spectral range of approximately 50 GHz, the instrumental width that resulted was approximately 1 GHz. Thus, if the heated-phonon bandwidth was significantly narrower than this, it could not be discerned by spectral scanning. One can circumvent this difficulty, however, by utilizing the special relationship between the frequency shift of the scattered light and the angle of scattering. From Eqs. (14) and (15) above, if the phonons at frequency ν_q have a bandwidth $\delta\nu_q$, then the scattered light will have an angular aperture $\delta\theta$ given by

$$\delta(\Delta\nu_i) = \delta\nu_q = (nv/c)\nu_i \cos(\tfrac{1}{2}\theta)\,\delta\theta \ . \tag{23}$$

Thus, by measuring the angular aperture $\delta\theta$ of the scattered Brillouin light associated with the heated phonons, one can determine the phonon bandwidth. This is done as illustrated in Fig. 6 by scanning with an aperture, whose opening is approximately 1.6 mm in the vertical direction and 6 mm horizontally, placed behind the 30-mm-diam collection lens. The frequency dispersion across the 6-mm horizontal distance is negligible. This aperture is best placed a distance f behind the lens equal to the focal length of the lens, for at this distance the light scattered at the same angle θ from all points along the laser beam path converges to a single point. In this way the source length accepted by the Fabry-Perot is not confused with angular width at the scanning aperture. In Fig. 7 is shown the intensity of the scattered light from the heated phonons vs vertical position of the aperture for sample MS-4A. The scale is such that 1 mm is related to an acceptance angle $\delta\theta$ which corresponds to a frequency width of 40 MHz. The effective half-width of the scattered light is 4.5 mm, which when convolved with the width of the aperture gives a half-width of approximately 4 mm or 160 MHz. The EPR linewidth in the [110] direction was approximately 500 MHz so that the phonon heating is occurring in a bandwidth that is less than one-half the EPR linewidth. This is in reasonable accord with expectation as mentioned earlier for an $S = 1$ three-level system in cubic symmetry. For full saturation of an inhomogeneous line in an $S = \frac{1}{2}$ system, one would expect the phonon bandwidth to be equal to the EPR linewidth. This has been verified by Valishev and Khasonov in cerium magnesium nitrate[12] and also in $CaWO_4$:Nd^{3+}.[13] The enhanced heating at line center will be seen to have even more dramatic consequences under special conditions to be described in Sec. V G.

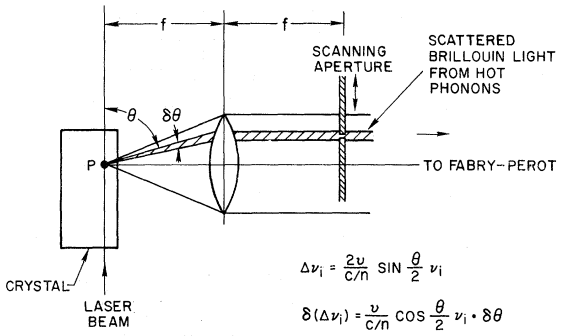

FIG. 6. Method of measuring the frequency width of the heated phonons by measuring the angular aperture $\delta\theta$ of the Brillouin-scattering light from these phonons. Aperture is typically 1.6 mm in vertical direction and approximately 6 mm in horizontal direction, perpendicular to plane of figure. The $\delta\theta$ associated with the hot-phonon bandwidth is smaller than the angular aperture of the lens.

C. Relaxation Profiles for Low-Velocity Transverse Phonons

When the resonant microwaves which maintain cw saturation of the spin system are rapidly switched off, the heated phonons must relax back to their thermal-equilibrium value; Fig. 8 shows a typical relaxation profile for the heated slow-transverse acoustic phonons obtained in this manner. For these measurements, the microwave power incident on the resonant cavity was square-wave modulated at rates of 40–400 Hz using an in-line microwave diode switch interposed between the free-running cw klystron and the microwave cavity. The Fabry-Perot interferometer was not swept but was adjusted to monitor continuously the peak of one of the Brillouin components of the heated ST phonons, and the recovery profile was recorded, when the microwaves were switched off, using the multichannel analyzer (MCA) synchronized to the diode switch modulation.

The observed phonon relaxation is characterized by a very rapid initial drop in the phonon excitation, which is beyond the fastest time resolution of 25 μsec of the MCA used, followed by a much slower return to equilibrium. Detailed studies of this long-time profile in our different samples show that the recovery is nonexponential for all readily observable times. The instantaneous decay times for the various samples are typically in the regime of a few milliseconds during this portion of the recovery observed with the MCA; this is significantly shorter than the asymptotic decay rate $T_1^{\rm obs}$ [see Eq. (12)] one would expect on the basis of the observed phonon heating under spin saturation. These results, however, are in agreement with the findings of our numerical solutions to the rate equations, Eqs. (6) and (7), which indicate that the phonon recovery proceeds at the asymptotic decay rate only at very long times, such that the spin system has almost returned to equilibrium. Under these asymptotic conditions, however, the very small phonon excitation makes its measurement by Brillouin scattering extremely difficult.

The most interesting portion of the decay lies in the very rapid decay at the very early times. In order to obtain the time resolution necessary to study this region of the decay, a time-to-amplitude converter (TAC) and a pulse-height analyzer (PHA) were incorporated into the experimental arrangement as shown in Fig. 9. Briefly, the TAC has the property that it produces an output pulse of amplitude proportional to the time difference between each of two pulses arriving at its start and stop inputs; the start pulse is coincident with the switching off of microwaves to the cavity and the stop pulse is derived from a photon incident on the phototube following microwave turn off. The output pulse of the TAC is then processed by the PHA

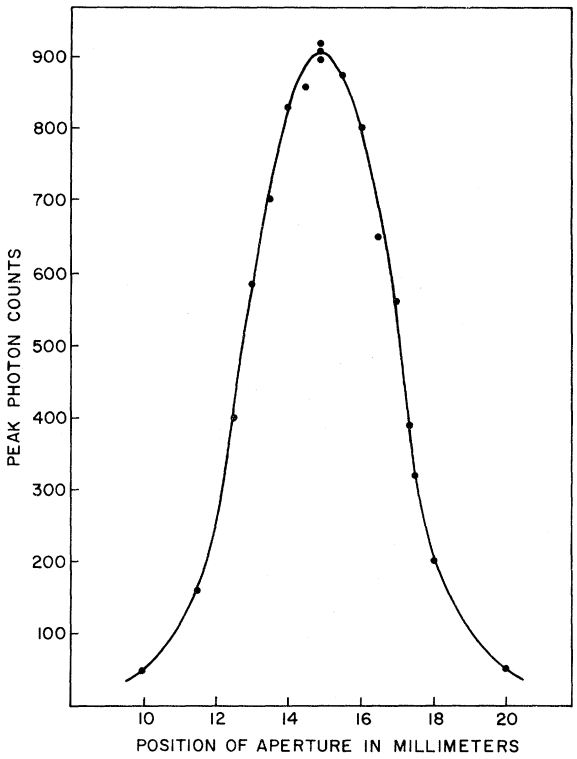

FIG. 7. Plot of photon counts from Brillouin-scattered light in Ni^{2+}:MgO associated with heated phonons vs vertical position of aperture (shown in Fig. 6). 1 mm of vertical scan of the aperture corresponds to a $\delta\theta$ which is equivalent to 40 MHz in phonon bandwidth. Thus, the heated phonons shown have a bandwidth of approximately 160 MHz compared to the ~500-MHz EPR linewidth and 900-MHz bandwidth of spontaneous Brillouin scattering subtended by the full lens aperture.

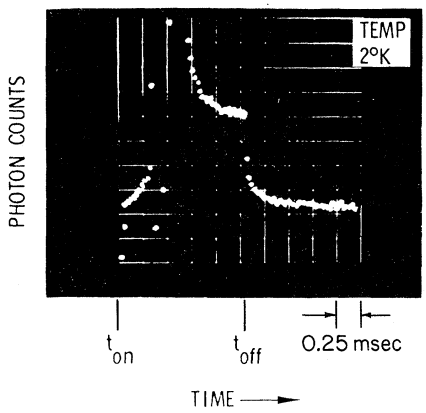

FIG. 8. Relaxation profile for heated low-velocity transverse phonons at a bath temperature of 2 °K. Saturating microwaves are switched on and off at times t_{on} and t_{off}, respectively; each major scale division is 0.25 msec. The rapid variations in phonon heating between t_{on} and t_{off} are due to strong cavity-pulling effects experienced when the spin system is driven from thermal equilibrium at 2 °K to saturation.

to give a histogram of the number of photons per unit time (scattered Brillouin light intensity) incident on the phototube vs time after microwave turn-off, or equivalently the time decay of the heated phonons. Our main requirement is that, following the initial start pulse to the TAC, the probability of more than one stop pulse arriving at the TAC during its active period (which is 30 μsec for our case) be negligible; otherwise, the statistics of the process become biased and the decay is distorted. Since this technique records a maximum of one photon for every microwave turn-off, the process must be repeated many times in order to obtain an accurate decay profile. For our measurements the microwave power was modulated at a 4–10-kHz rate and the data were collected over a period of several minutes.

Typical early-time decay profiles for two MgO: Ni^{2+} samples (MS-2C and MS-4A) are shown in Fig. 10(a). The decay begins with essentially zero slope, quickly speeds up over a period of a few microseconds, and then slows down again in its approach to equilibrium; the decay profiles for the Stokes and anti-Stokes components in a given sample were found to be identical. This behavior is in good agreement with the qualitative features of the curves of Fig. 1 obtained from numerical solutions to the rate equations, Eqs. (6) and (7). For example, note that after the initial rapid decay sample 4A, which has the larger σ, reaches a lower fraction of its initial excitation as compared to 2C.

We saw above that a phonon heating corresponding to a bottleneck factor $\sigma \sim 2\times10^3$ was observed for sample MS-4A. This value of σ was not far from the value of 0.8×10^3 which was estimated using $\tau_{ph} \simeq 5$ μsec and $T_{1D} = 10^{-3}$ sec. Thus, with these values for this sample, $\sigma\tau_{ph}/T_{1D} \approx 10 \gg 1$ and one expects the initial rapid decay to proceed exponentially with time over at least half a decade with a time constant equal to τ_{ph}, as indicated earlier in Sec. II. In Fig. 10(b) is shown a semilog plot of the phonon relaxation for sample 4C corresponding to Fig. 10(a). The extended region of exponential decay in Fig. 10(b) corresponds to a time of 5.4 μsec which we may label τ_{ph} as it is consistent with the condition $(\sigma\tau_{ph}/T_{1D}) \gg 1$. While a somewhat less extended region of exponential decay of very similar time constant is observed for 2C, we must recall that the observed heating, or σ, for 2C is seven times smaller than for 4A. In view of the fact that such factors as Ni^{2+} concentration, sample size, EPR linewidths, etc. were the same for both samples we can at this time only ascribe this difference to the fact that τ_{ph} is approximately seven times shorter, i.e., ~0.8 μsec, in sample 2C. (Possible reasons for this will be cited below.) For sample 2C, $(\sigma\tau_{ph}/T_{1D})$ ~0.2 so that the fast region of decay no longer corresponds to τ_{ph}, and a direct determination as in the case of 4A is not possible. In fact, numerical solutions of the two-level system with parameters corresponding to 2C show a small region of exponential decay (although less pronounced) with a decay time approximately six times τ_{ph} (τ_{ph} now about 0.8 μsec), which is again consistent with observation. While the numerical calculations referred to are for a two-level system, the essential conclusions regarding τ_{ph} should apply in a semiquantitative fashion to a three-level system as well. Similar calculations for a three-level

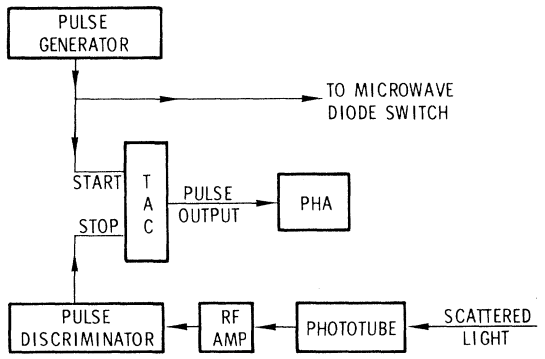

FIG. 9. Experimental arrangement for measuring phonon-decay profiles with fast-time resolution. The pulse generator controls the switching on and off of the saturating microwaves to the sample and also provides the start pulse to activate the time-to-amplitude converter (TAC). The stop pulse for the TAC is derived from a scattered light photon incident on the phototube following microwave turnoff. The amplitude of the output pulse from the TAC is processed using a conventional pulse-height analyzer (PHA) (see text).

system are far more complex and bring additional parameters into the problem without changing the major physical features.

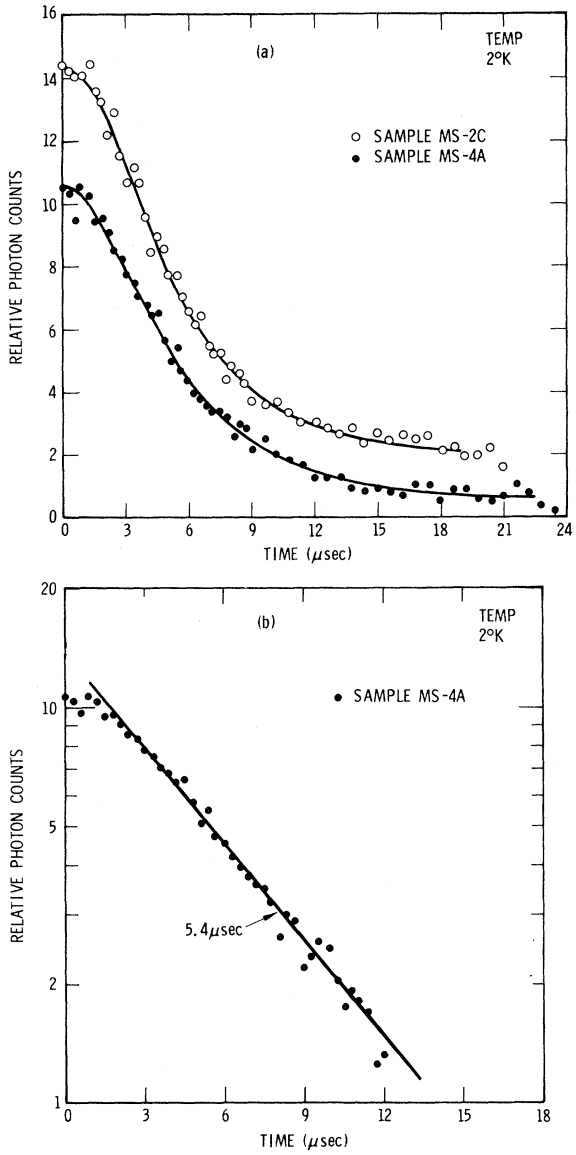

FIG. 10. Typical early-time decay profiles, obtained with system shown in Fig. 9, of heated phonons for $MgO:Ni^{2+}$ samples at an ambient temperature of 2 °K. (a) Experimental points are for heated low-velocity transverse phonons; solid curves are fits to the data. Sample MS-4A actually shows the larger phonon heating, as described in the text, under cw microwave saturation; i.e., ordinate scale of relative counts refers only to an individual curve. Important comparative features between curves are had by normalizing curves for both samples to same point at $t=0$. (b) Semilog plot of the data of (a). Solid line is exponential fit to the rapid decay and indicates a phonon lifetime $\tau_{ph} \simeq 5.4\ \mu$sec for MS-4A. Note the extended region of exponential decay for sample MS-4A. See text for discussion of lifetime of MS-2C.

In the He-temperature region, microwave phonon decay via anharmonic processes is essentially inoperative (nonresonant impurity scattering from Ni^{2+} plays no role either), as will be discussed in Secs. V D and V E. In the absence of intrinsic anharmonic decay processes, the lifetime of the particular class of heated phonons under observation is determined by phonon-mode conversion at the crystal boundaries to other modes at the same frequency which, however, do not couple to the spins and by leakage of phonons out of the crystal at the sample surface following many internal reflections. Sample MS-2C was observed to have some cracks running through it to the surfaces and in general showed greater regions of strain, under examination by crossed polarizers, as compared to MS-4A. Thus, it is very plausible to assume that the smaller phonon lifetime in 2C compared to 4A is due to these cracks and poorer surface quality. Deterioration of surface quality with time and handling in both these crystals resulted in smaller observed phonon heating.

The fact that the heated phonons under view have two nonintrinsic alternate paths for leaking away, i.e., mode conversion at boundaries or leakage out of the crystal, each of which may have different characteristic times and which also represent decay towards different equilibrium values, calls for additional caution in attempting to extract a precise single τ_{ph} for the decay. As will be demonstrated below in Sec. V E, for example, some phonons are selectively heated by the spins as compared to others at the same frequency. Thus, when the microwaves are switched off, the differentially heated phonons at the same frequency will tend to approach some common temperature by mode conversion upon reflection at the crystal boundaries. This may be viewed as a cross relaxation among the phonons at the same frequency and could proceed at a different rate $1/\tau_{CR}$ than the leakage of the heated phonons from the crystal into the helium bath $1/\tau_l$. In this case, τ_{ph} for the phonons under observation should be characterized by the two time constants τ_l and τ_{CR} and an extended region of a single exponential decay is anticipated only if the two times are significantly different or very close to each other. As to the relative magnitudes of τ_l and τ_{CR}, the mere fact that phonons at the same frequency are selectively heated with steady-state microwave saturation (see Sec. V E) implies that τ_{CR} cannot be very much faster than τ_l, or $\tau_{CR} \gtrsim \tau_l$. Of course, there is no unique τ_{CR} either, since some phonons may cross relax with ease by mode conversion, even upon *specular* reflection at the boundaries, while the slow-transverse phonon whose decay is shown in Fig. 10(a) will not mode convert upon specular reflection for the geometry used (see Sec. V E).

Let us first assume that $\tau_l < \tau_{CR}$ so that the τ_{ph} determined from Fig. 10 corresponds to τ_l, the escape time of the phonon from the crystal. The $\tau_{ph} = 5.4$ μsec in MS-4A, with $v = 5.34 \times 10^5$ cm/sec, corresponds to a phonon mean free path of 2.9 cm. Taking an average distance of travel of 3 mm between reflections and using the mean free path of 2.9 cm, we see that the phonon suffers approximately ten reflections before its intensity decays to $1/e$ or approximately a 10% loss upon each reflection. But from where is this loss to come? Since this transverse phonon does not propagate in the liquid helium, it will suffer total internal reflection for specular reflection without mode conversion. Even if there is mode conversion to longitudinal waves due to surface imperfections, the acoustic impedance mismatch between MgO and liquid He is such that no more than 1% of the energy in the longitudinal phonons should be transmitted to the helium upon each reflection. Thus, if it is τ_l which is being observed, it is much faster than what one expects from leakage due to normal acoustic mismatch at a perfect surface. This is a familiar observation with regard to phonons of frequency above 10 GHz that has been encountered many times before in a number of different contexts. Mims and Taylor have reached similar conclusions with regard to τ_l in their study of a microwave-phonon bottleneck in Ce-doped lanthanum magnesium nitrate.[6] Sabisky and Anderson have also found that, above 10 GHz, τ_l is smaller than that which is expected from acoustic mismatch.[27] An anomalously small τ_l is also implied by the observed Kapitza resistance (which is associated with heat transport by phonons out of the crystal) at the interface between solid and liquid He which is invariably found to be smaller than anticipated.[28]

Many reasons have been advanced to explain this short τ_l, such as surface irregularities and strains, which would somehow scatter out more energy into the He. The surface irregularities of the crystals used in our experiments have dimensions which are smaller than the acoustic wavelength, however. In water crystals, cracks and inclusions of water may be present so that the distance the phonon travels before boundary reflection is considerably smaller than the bulk dimensions of the crystal.[6] One might also imagine several layers of solid He adhering to the crystal which may serve as an impedance transformer to the He. The setting up of surface waves which couple to the liquid may also play a role. In any event, we certainly cannot provide any clarification of the origin of a short τ_l from our experiment. Given the fact of a fast τ_l, however, which involves so many uncertainties as to what happens at the boundary, one cannot rule out the possibility that there is a considerable degree of mode conversion as well, above what is expected from specular reflection. This could mean that τ_l and τ_{CR} may be nearly the same and the τ_{ph} observed is some mixture of these times whose difference cannot be resolved in our experiment. It would also be helpful to extract τ_{ph} from the heated phonons by observing their unhindered decay without coupling to the spin system, by using a magnetic field pulse to detune the spins from the phonons during the decay. However, this would require the switching of several hundred gauss in one μsec. We are unable to make more definite statements until, in addition, the decays of different heated phonons at the same frequency are observed, and this is difficult in our current experimental configuration. This question of phonon decay and mode conversion will be returned to in Sec. V E.

In the way of apology we anticipate a variety of questions that immediately arise from the picture we have outlined for phonon decay. For example, if phonon lifetime is governed by boundary conditions, then changing sample size or quality of the surface should change τ_{ph} and the degree of heating. In this connection we have observed a decrease of heating in samples where surfaces have visibly deteriorated through handling and accumulation of grit, as mentioned. Repolishing and cleaning of these surfaces have again increased the heating although no quantitative statements can be made. As for sample size, we are restricted on the low end to dimensions of roughly a few mm per side in an effort to minimize elastic light scattering and to similar dimensions on the high end by frequency-pulling effects on the microwave cavity. Experiments to check size effects are in progress but are difficult as one must ensure that other parameters that govern τ_{ph}, such as concentration, degree of saturation, surface quality, etc., remain the same.

D. Variation of Phonon Heating with Crystal Temperature

We now wish to examine the degree of steady-state heating of the microwave phonons by the saturated relaxing spins as a function of the ambient temperature of the crystal. Turning to Eq. (10) we ask for the temperature dependence of each term in this expression for the phonon heating. $n_1^0 - n_2^0$ varies as $\tanh(\hbar\omega/2kT)$ or inversely as T (for $\hbar\omega \ll kT$). T_{1D} also varies as $\tanh(\hbar\omega/2kT)$ for the direct process. In this connection it must be emphasized that even as we go to higher temperatures and a Raman relaxation rate may begin to exceed the direct process rate, the appropriate T_{1D} to use in Eq. (10) is the unbottlenecked direct-process T_{1D} as long as we *saturate the spin system*. In other words, we are concerned with the rate at which direct-process phonons are being produced, and this is independent of the fact that a parallel and faster Raman process might be relaxing the

spins. The presence of a faster Raman process simply makes it that much more difficult to saturate the spin system but obviously does not alter the direct-process T_{1D}. (Incomplete saturation means that something smaller than $n_1^0 - n_2^0$ is appropriate in the expression for σ.) $\rho(\nu_0)\, d\nu_0$ is independent of T in the temperature range that the bottleneck was studied, i.e., between 2 and 40 °K. The last factor, the phonon lifetime τ_{ph}, as discussed earlier, is not governed at the lowest temperatures by intrinsic anharmonic decay processes but rather by mode conversion and leakage of the phonons out of the crystal at the surfaces after many reflections. The temperature at which the intrinsic τ_{ph} (determined by three-phonon decay) becomes significant compared to the τ_{ph} determined solely by boundary effects can be estimated from the experiments of Pomerantz,[29] who found that the attenuation of the slow-transverse acoustic phonons at 9 GHz was less than 3 dB/cm at 40 °K and was varying with temperature as T^4; so that it is quite negligible at temperatures below 35 °K. The attenuations for the fast-transverse and longitudinal phonons were found to be even smaller. We can extrapolate these results to the 26-GHz transverse waves in our experiments by assuming that the attenuation $\alpha \sim \omega T^4$, as derived by Landau and Rumer[30] and verified by Pomerantz[29] in the frequency range 3–9 GHz. Thus, the attenuation at 25 GHz should be approximately only three times stronger than Pomerantz's values at 9 GHz, implying that up to 35 °K phonon mean free paths in our experiments due to anharmonic processes should be very much greater than our crystal dimensions so that τ_{ph} is determined by crystal dimensions and independent of T. *To the extent therefore that τ_{ph} and $d\nu_0$ are independent of T and the spin system is saturated, the phonon heating should be independent of T* since T_{1D} and $n_1^0 - n_2^0$ both vary as $\tanh(\hbar\omega/2kT)$.

In Figs. 11(a) and 11(b) are shown the thermal Brillouin spectra at crystal ambient temperatures of 24 and 37 °K, respectively. The scattering geometry and basic experimental configuration are similar to that discussed earlier in connection with Fig. 4. The only modification was the introduction of a controlled flow of cold He gas around the sample from a liquid-helium storage vessel to obtain these higher temperatures. The temperature was monitored by various resistance thermometers located in different regions of the microwave cavity.

Figures 11(c) and 11(d) show the corresponding spectra to (a) and (b) with resonant saturation of the Ni^{2+} spin system by microwaves. It is immediately apparent that again the 26-GHz phonons are significantly heated at 24 °K and to a lesser extent even at 37 °K. Note that as before this heating is selective as there is no apparent heating of the phonons at 31 GHz.

In Fig. 12(a) is ploted the excess heating ΔT above thermal equilibrium of the resonant 26-GHz phonons as a function of sample temperature. The point in the crystal from which the scattering was observed was such that the Stokes line was greater than the anti-Stokes. (This anomalous asymmetry between the Stokes and anti-Stokes intensities of the heated phonons occurs in localized regions of the crystal and will be further discussed in Sec. V G.) A similar plot is shown in Fig. 12(b) of the scattering from a different region of the crystal in which the anti-Stokes intensity was greater than the Stokes. While both figures display a decrease of heating with increasing temperature T, the point to be emphasized is the very *slow* variation with T of the excess phonon heating ΔT, which is seen to be almost constant from 8 to 16 °K, thus verifying the essential constancy of the phonon heating and the fact that τ_{ph} is not intrinsic. The decrease in ΔT over most of the range plotted is seen to be certainly slower than $1/T$, while any intrinsic phonon-decay time would be expected to have a $1/T^4$ dependence.[30] The actual observed decrease in ΔT is attributed to the greater difficulty in saturating the microwave transition with increasing T due to a speedup in T_1 arising from a competing Raman process. Even at 8 °K we found that with our maximum applied microwave power the degree of saturation of the spin system was somewhat less effective as compared to 2 °K. The 2 °K data are not

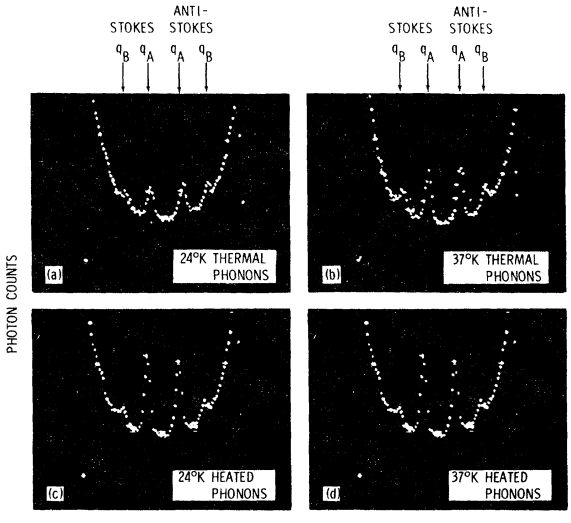

FIG. 11. Brillouin-scattered light from microwave-phonon bottleneck at elevated temperature, corresponding to same configuration shown in Fig. 4. Frequencies of $\tilde{q}_A$ and $\tilde{q}_B$ are the same as in Fig. 4. (a) and (b) show thermal scattering with microwaves off while (c) and (d) show the heated phonons $\tilde{q}_A$ at 25.6 GHz when the saturating microwaves are on.

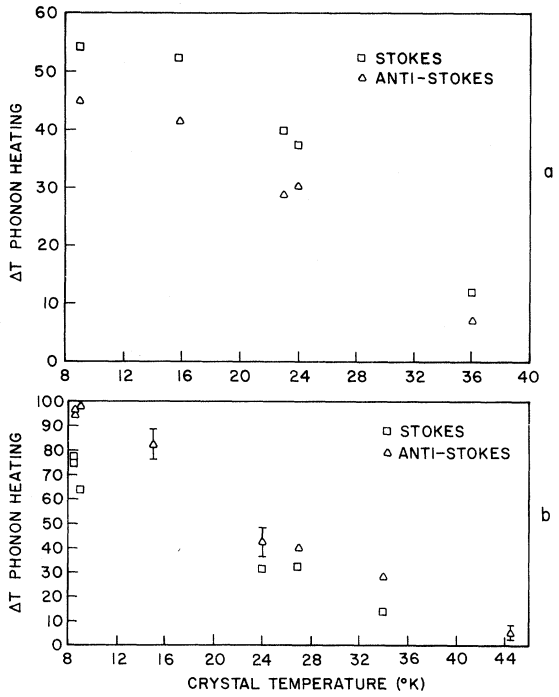

FIG. 12. Incremental peak phonon heating (uncorrected for bandwidth) vs crystal ambient temperature. (a) corresponds to a point in the crystal where Stokes intensity of heated phonons is larger than anti-Stokes, while (b) corresponds to a different point where the intensity is reversed. The relatively slow variation of ΔT with crystal ambient temperature is indicative of the fact that τ_{ph} is independent of temperature and not governed by intrinsic anharmonic decay processes in this temperature range.

plotted here as they were taken under different experimental conditions below the λ point of He and there would be a large error in attempting to correlate them with the temperature points shown here. ΔT at 2 °K was roughly a factor of 1.5–2 larger than at 8 °K. Of course the drop in ΔT vs T seen at the higher temperatures will also reflect the coming into play of intrinsic phonon-decay processes at approximately 30–40 °K in accord with the data of Pomerantz[29] cited above.

We further emphasize that, even in a crystal with such a high impurity concentration as 1% Ni, the wavelength of the phonons is so much longer than the mean distance between the impurities that *impurity scattering is completely ineffective.* While there are, of course, Fourier components of the fluctuations in impurity concentration at the phonon wavelength which could scatter, their amplitude is very low. This conclusion is further borne out in heat-pulse experiments on these same crystals by Narayanamurti and Chin[31] involving phonons of even shorter wavelength. Further evidence for the fact that τ_{ph} is neither intrinsic (three-phonon scattering) or impurity dependent, but is primarily governed by crystal surface geometry and leakage out of the crystal after many reflections, will be given in Sec. V E, where experimental evidence will be cited for mode conversion of the phonons upon reflection at the crystal boundaries.

E. Brillouin Scattering from Longitudinal Phonons with Zero Spin-Phonon Coupling

Until now, our discussion has been based on the observation of resonantly heated 25.6-GHz slow-transverse (ST) phonons traveling in a particular direction in the crystal, i.e., those phonons labeled $\vec{q}_A$ in Fig. 4. The reasons for selecting this particular phonon for observation have been given earlier in terms of expectation of a significant bottleneck connected with strong spin-phonon coupling and other favorable experimental conditions related to the light scattering. The question immediately arises as to the degree of heating of other 25.6-GHz phonons. In particular, for a dc magnetic field applied perpendicular to the $(1\bar{1}0)$ scattering plane shown in Fig. 4, $\Delta m_s = -1$ spin transitions will not generate any phonons traveling in this plane whose polarization also lies in this plane, i.e., longitudinal and fast transverse, as is shown in the Appendix. Therefore the observation of any "hot" longitudinal phonons traveling in this plane would be suggestive of mode conversion at the boundaries from other heated 25.6-GHz phonons which do couple to the spins.

The observation of longitudinal phonons (L) at 25.6 GHz in the $(1\bar{1}0)$ scattering plane required a more acute scattering angle of 48.6° because of the larger sound velocity. As it was inconvenient to achieve this angle by changing either the angle of the incident laser beam or the direction of viewing, the technique shown in Fig. 13 was adopted to simultaneously view the 25.6-GHz ST and L phonons. A 20.7° bevel was cut on the face of a crystal, which was similar in concentration and orientation to those samples described until now as shown in Fig. 4. The laser beam, upon reflection from the beveled surface, now made the necessary angle of 48.6° with the viewing direction for the observation of the longitudinal phonons. By viewing along the line shown (corresponding to the Fabry-Perot axis) we therefore simultaneously observe light scattered from points A and B, defined by the intersection of the laser beam with the Fabry-Perot axis. The appropriate scattering triangles for these points are shown in Fig. 13. Fortunately, the scattered light from point A corresponding to the ST phonon $\vec{q}_A$ is polarized at right angles to the scattering plane whereas the scattered light from B associated with the longitudinal phonons $\vec{q}_B$ is polarized in the scattering plane. Thus by means

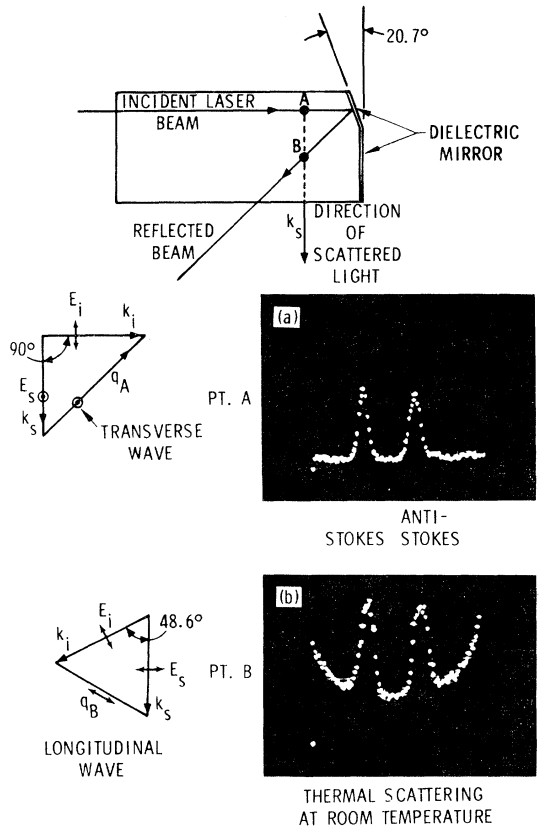

FIG. 13. Configuration of 1% Ni^{2+}:MgO crystal used to observe simultaneously 25.6-GHz ST and L phonons. Scattering triangle for incident laser beam is shown to left of (a) and selects a value of $\vec{q}$ which corresponds to 25.6-GHz ST phonons. Appropriate scattering diagram for reflected laser beam is to left of (b) and corresponds to a shallower scattering angle and smaller $\vec{q}$, such that the longitudinal phonons at this reduced $\vec{q}$ are also at 25.6GHz. Polarizations of scattered light in (a) and (b) are at right angles to each other so that one may view either transverse phonons at point *A* or longitudinal phonons at point *B* by 90° rotation of polarizer in the path of the scattered light.

of a linear polarizer either the ST phonons or L phonons can be selected for observation. As the laser beam reflected from the mirror on the bevel was further internally reflected several times before emerging from the sample, the elastically scattered light was inordinately large. To eliminate this large amount of elastically scattered light, an iodine-vapor filter was used which selectively attenuated the laser light as described elsewhere.[32]

The room-temperature thermal Brillouin spectra corresponding to phonons $\vec{q}_A$ and $\vec{q}_B$ are shown alongside their appropriate scattering triangles in Fig. 13. The larger bandwidth of the L phonons is a result of the larger sound velocity v and the shallower scattering angle θ; i.e., for the same angular aperture of collected light $\delta\theta$ the bandwidth of the collected light is proportional to $\delta\theta\, v \cos\frac{1}{2}\theta$. The scattering intensity of the L phonons is approximately 20% greater than the ST phonons.

At 2 °K, the intensity of the thermal Brillouin scattering decreases by approximately a factor of 150 and would be unobservable for the integration time used in Fig. 14, where the heating of these phonons by the microwaves is shown. The particular point of observation chosen, point *A*, was such that, for the transverse phonons, the Stokes line was more strongly heated than the anti-Stokes. (As mentioned earlier and detailed in Sec. V G, the disparity in Stokes and anti-Stokes lines is associated with localized anomalous ST phonon heating.) The average phonon heating, uncorrected for bandwidth, was approximately 150 °K or ~700 °K with the bandwidth correction. Figure 14(b) shows the corresponding "anomalous" heating observed for the longitudinal L phonons. While the heating of these L phonons is smaller by a factor of 2–4 compared to that of the ST phonons $\vec{q}_A$, it is nonetheless anomalous since these L phonons do not couple directly to the spins as pointed out above. It is most reasonable to ascribe this observed heating of the L phonons to mode conversion upon

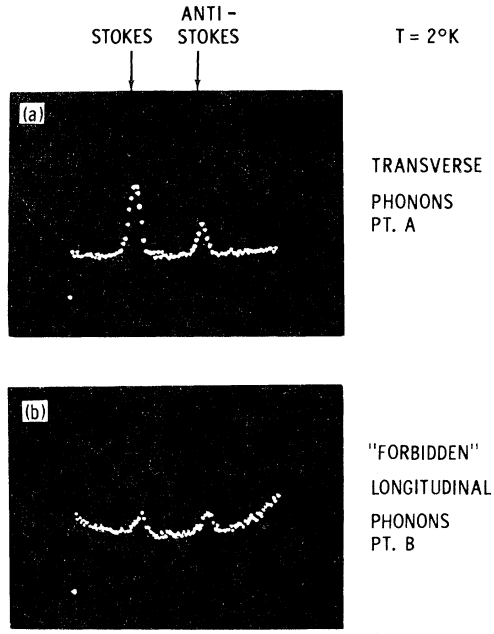

FIG. 14. Same configuration as Fig. 13 except that crystal temperature is now at 2 °K. For integration time used here thermal Brillouin scattering cannot be seen and is below the noise. (a) shows the heating of the transverse phonons upon microwave saturation. The asymmetry in heating of Stokes and anti-Stokes is discussed in text. (b) shows heating of the longitudinal phonons at same frequency to which the spins do not directly couple. Observed heating is ascribed to mode conversion from other heated phonons which couple to the spins.

reflection at the crystal surfaces by those phonons which do directly couple to the spins. However, before discussing the mode conversion in more detail, we will briefly consider some alternate explanations for the heating and show that they completely fail to explain the observed heating of the L phonons.

1. Breakdown of Selection Rules

a. Crystal misalignment and solid-angle effects. Crystal misalignment of a few degrees ($\delta\varphi$ in radians), such that the applied field H is not precisely perpendicular to the $(1\bar{1}0)$ plane, will allow the $\Delta m_s = 1$ longitudinal phonon coupling, but its intensity will be down roughly by $(\delta\varphi)^2$ compared to the allowed transverse phonon. Similarly, a misalignment of the laser beam by a small angle $\delta\varphi$, so that phonons outside the $(1\bar{1}0)$ plane are being viewed, will also be negligible. In the same vein, while our collection optics has a finite f number, it is nonetheless quite large, corresponding to a range of scattering angles of only a few degrees in the sample, so that again we observe phonons within a few degrees of the $(1\bar{1}0)$ plane.

b. Breakdown of spin-phonon-coupling selection rules due to static random strains. Static random strains may lower the cubic symmetry at the Ni^{2+} site and provide *state mixing* of the $|\pm 1, 0\rangle$ states, which are labeled by magnetic field quantization. Such a mixing of $\langle \pm 1|$ states would allow the quadratic spin operators in $\mathcal{H}_p$ (see Appendix) to make "forbidden" $\Delta m_s = 1$ transitions. However, a measure of the random static D and E terms produced by local strains is provided by the observed inhomogeneous Ni^{2+} linewidth of 150 G, which is far smaller than the applied magnetic field of 8000 G. The state mixing produced by these lower symmetry fields is of the order of $D/g\beta H$ and is therefore quite negligible as evidenced by the orders-of-magnitude lower intensity observed for the $\Delta m_s = 2$ electromagnetic EPR transitions compared to the $\Delta m_s = 1$ transitions in this crystal.

The random strains also *modify the over-all cubic symmetry of the dynamic spin Hamiltonian* and split, for example, the Γ_5 representation (see Appendix). Additional constants are thereby introduced; i.e., the single constant G_{44} is no longer appropriate to $\mathcal{H}_4$ and $\mathcal{H}_6$ and the cancellation of $a_4\mathcal{H}_4 + a_6\mathcal{H}_6$ discussed in the Appendix would no longer hold, so that $\mathcal{H}_4$ and $\mathcal{H}_6$ separately produce $\Delta m_s = 1$ longitudinal phonons. However, if other constants were needed due to random local strains which lower the site symmetry, this would reveal itself as an *additional* broadening of the EPR line upon the application of static stress in measuring the G tensor. Any extra broadening observed is usually far less than the shifts or splittings seen so that a breakdown of the selection rules from this source may be discounted.

An alternative argument can be made for the negligible effect of lower-symmetry elements in the dynamic strain tensor. In those cases where the crystal structure is such that local site symmetries are characterized by large departures from cubic symmetry, such as the Al^{3+} site in Al_2O_3, it is found that the extra constants G_{ij} (or their difference from cubic symmetry) needed to describe the strain effects on an impurity ion, such as Cr^{3+} in Al_2O_3,[33] are of the same order of magnitude or much less than the G_{11} and G_{44} appropriate to cubic symmetry, i.e., Cr^{3+}:MgO.[25] Now, if the low-symmetry fields in Al_2O_3 produce a given D splitting and corresponding random strains produce splittings of order D', we would expect the ratio of the extra G_{ij} terms due to random strains compared to the G_{11} and G_{44} in cubic environments to be $\sim D'/D$. A measure of D' is had from the inhomogeneous linewidth.[34] Thus, for example, in Ni^{2+}:Al_2O_3, $D' \sim 10^{-2}$ cm^{-1} and $D \sim 1$ cm^{-1}. Thus, we expect the noncubic G_{ij} terms due to the random local strains to have a negligible effect on the forbiddenness of the $\Delta m_s = 1$ transitions in our geometry.

c. Dynamic spin-phonon Hamiltonian linear in spin, i.e., $\mathcal{H}' \sim \vec{H} \cdot \tilde{\tilde{G}}' \cdot \vec{S}$. Here $\tilde{\tilde{G}}'$ is the dynamic g tensor. As discussed in the Appendix, the magnitude of this term compared to the quadrupolar term quadratic in S is of the order of $g\beta H/\lambda$, i.e., the Zeeman energy divided by spin-orbit coupling energy, which is approximately 10^{-2}–10^{-3} and is therefore completely negligible here.

2. Mode Conversion upon Boundary Reflections

Neither *a*, *b*, or *c* above would therefore seem to be at all capable of significantly relaxing the spin-phonon selection rules, and the observation of the "forbidden" $\Delta m_s = 1$ longitudinal phonons is undoubtedly connected with mode conversion at the boundaries.[35] However, it seems that in our case this can only occur for *non*specular reflection. For example, while a transverse phonon polarized in the scattering plane will convert, upon specular reflection from a crystal face, into transverse and longitudinal phonons as shown in Fig. 15,[36] this transverse phonon polarized in the $(1\bar{1}0)$ scattering plane does not couple to the spins either, as shown in the Appendix. Only the slow-transverse phonons polarized *perpendicular* to the $(1\bar{1}0)$ light-scattering plane couple to the spins, and for specular reflection they return back into the plane with the *same* polarization, as the crystal faces are perpendicular to this plane. Any other heated phonons which do not travel in the scattering plane cannot be specularly reflected into this plane for the crystal geometry used. Thus, if the heating of the longitudinal phonons is to be ascribed to mode

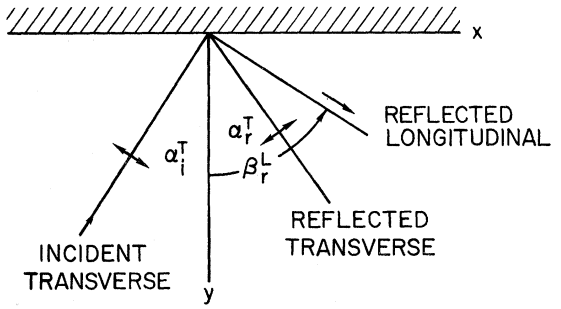

FIG. 15. Illustration of conversion of transverse phonon to transverse and longitudinal phonons upon specular reflection at a boundary. See text and Ref. 36.

conversion, it may arise from heated phonons traveling outside the plane and partially *non*specularly reflected as longitudinal phonons into the plane. In addition, intraplane mode conversion connected with boundary strains and imperfections (such as was mentioned earlier in Sec. V C to explain a τ_1 that was considerably faster than anticipated from acoustic mismatch between the crystal and the helium) may be playing a role. It is difficult to make a quantitative statement about the relative amounts of specular and nonspecular reflection. However, since our phonon wavelength is the same as that of the light used, we might guess that the ratio of specularly reflected to diffusely reflected light at the surfaces of this crystal would be quite a bit smaller than a similar ratio for the phonons because of the larger impedance mismatch at the surface for sound as compared to light. The small amount of diffusely scattered light that is seen indicates, however, even following this reasoning, that most of the phonon energy would be specularly reflected and therefore a number of reflections would be required to produce the heating of the longitudinal phonons. This is consistent with the phonon-decay-time observations described earlier in Sec. V C and the persistence of the bottleneck at higher temperatures as discussed in Sec. V D, which also underlined the very long life of the phonons. The long intrinsic phonon lifetime allows many reflections from the crystal surfaces before escape to the bath. These boundary reflections serve as a phonon cross-relaxation mechanism and tend to produce a certain degree of equilibration between all the phonons at the same microwave frequency. If one were to observe the decay of the "forbidden" longitudinal phonons whose heating was described above, then presumably their decay would reflect feeding or cross relaxation from the more strongly heated phonons. However, the lower level of excitation of the longitudinal phonons coupled with the very intense elastic light scattering in the sample precluded measuring the decay of these phonons.

In spite of the presence of phonon cross relaxation, we must emphasize the different degree of heating for different phonons at the same frequency, i.e., the longitudinal and slow-transverse phonons, as described above. Selective heating of different phonons appears even more forcefully in the asymmetric heating of the Stokes and anti-Stokes lines in certain regions of the crystal as will be discussed in Sec. V G.

F. Heating of Longitudinal Phonons due to $\Delta m_s = 2$ Spin Transitions

Our basic experimental arrangement was selected in order to observe the heating of ST phonons which are directly coupled to the $\Delta m_s = 1$ spin transitions. As was pointed out earlier, however, it would also be of interest to study the heating of phonons at frequency 2ν produced by $\Delta m_s = 2$ spin transitions when the spin system is being pumped at the frequency ν of the $\Delta m_s = 1$ transitions. In particular, we show in the Appendix that, for the chosen $(1\bar{1}0)$ scattering plane and an applied $[1\bar{1}0]$ magnetic field, the ST mode couples only to $\Delta m_s = 1$ transitions while the fast-transverse and L modes couple solely to $\Delta m_s = 2$ transitions. Thus, the observation of ST phonon heating at ω and, for example, L phonon heating at 2ω should provide information on the relative role of the various resonant phonons in the dynamics of a strongly bottlenecked system.

The simultaneous observation of Brillouin scattering from ST and L phonons at ω and 2ω, respectively, requires that the sound velocity of the longitudinal mode be twice that of the ST mode for a given phonon propagation direction. For the chosen $(1\bar{1}0)$ scattering plane, this 2-to-1 ratio of the sound velocities cannot be realized exactly, although it is most nearly satisfied for ST and L phonons propagating along the [110] crystal direction. As is evident from the scattering diagram of Fig. 4, these [110] phonons can be readily probed by observing the light $\vec{k}_s$ scattered from phonons $\vec{q}_A$ when the scattering angle is reduced from our usual 90° value. Then, by varying the angle of incidence of the input laser beam, while keeping the collection optics fixed, one can obtain slightly different input-beam geometries which allow separate, but relatively easy, monitoring of ST and L phonons at ω and 2ω exactly.

The modifications to our basic scattering geometry are schematically depicted in Fig. 16(a); a pair of mirrors is inserted between the MgO sample and the Fabry-Perot interferometer and positioned so as to view the Brillouin-scattered light for a scattering angle of ~85° in the sample. In Fig. 16(b), we show a room-temperature spectrum for the ST and L modes arising from the

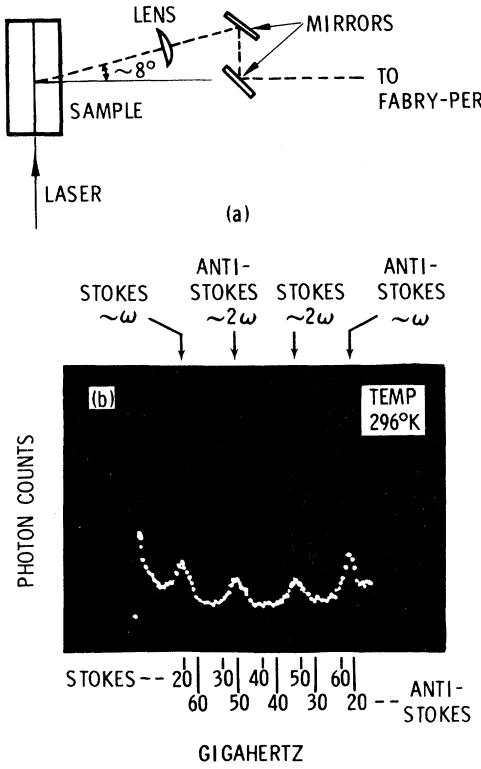

FIG. 16. Thermal Brillouin scattering at room temperature from low-velocity transverse and longitudinal phonons in MgO:Ni^{2+} at frequencies ν and 2ν, respectively. (a) Modification of the 90° scattering geometry of Fig. 3 to view phonons propagating along the [110] crystal direction. Inclusion of the mirrors allows monitoring of these phonons without changing sample orientation or interferometer position. (b) Room-temperature Brillouin spectrum of the low-velocity transverse ($\sim\omega$) and longitudinal ($\sim 2\omega$) phonons using the configuration of (a). Incident laser beam is normal to the dielectric mirror deposited on the sample. Upper and lower frequency scales refer to Stokes and anti-Stokes lines, respectively.

input laser beam, which is incident normal to the dielectric mirror deposited on the sample; here again, the Fabry-Perot spacing has been suitably adjusted to place the spectra between adjacent orders of the Rayleigh line. The frequencies of these modes are still not harmonically related, nor will they be at a 2 °K ambient temperature either; however, as stated above, slight variations of the laser angle of incidence away from the normal will permit a study of these modes at exactly the required frequencies.

Figures 17(a) and 17(b) show typical spectra for the heating of the ST and L phonon modes with microwave saturation of the spin transitions at 23.85 GHz for a bath temperature of 2 °K. Microwave saturation is occurring at the center of the $\Delta m_s = 1$ spin resonance line where the ω-phonon heating is largest; the ST and L mode spectra are obtained for scattering angles of ~79.5° and ~85°, respectively. The peak scattering intensity for the L mode indicates initially an effective phonon temperature, uncorrected for bandwidth, of ~50 °K. A direct comparison of Fig. 17(b) with the spectrum of Fig. 16(b) shows, however, the heated 2ω-phonon linewidth to be noticeably less than the observed L-mode linewidth at room temperature. The observed linewidth for the heated phonons is undoubtedly limited by the bandpass of the Fabry-Perot interferometer (~2 GHz for this plate spacing), whereas the room-temperature linewidth is determined by the combined bandpasses of the input collection lens and the Fabry-Perot; thus, the phonon temperature of 50 °K is only a lower bound and could easily be an order of magnitude or more greater, when the peak intensities are suitably

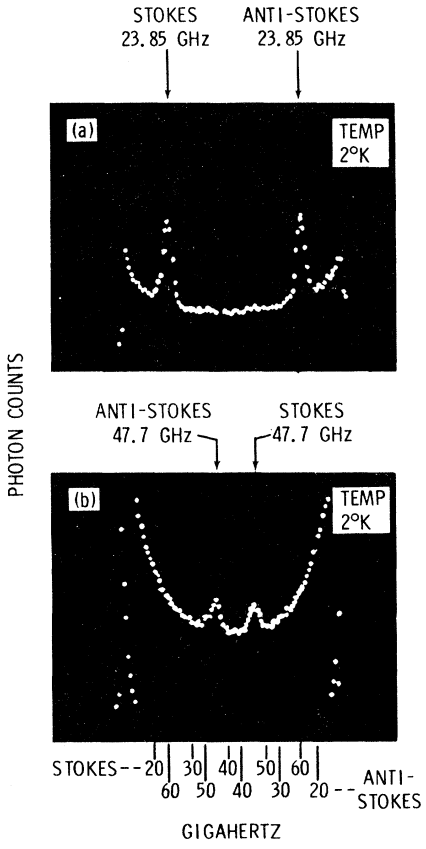

FIG. 17. Brillouin scattering from heated transverse and longitudinal phonons in MgO:Ni^{2+} at a bath temperature of 2 °K. Microwave saturation of the Ni^{2+} spin transitions occurs at 23.85 GHz in an applied field of ~7700 G. (a) Scattering from heated low-velocity transverse phonons at 23.85 GHz. (b) Scattering from heated longitudinal phonons at 47.7 GHz. The spectra of (a) and (b) were obtained with different input-laser-beam orientations, but fixed collection optics; the narrow bandwidths of the heated phonons account for the inability to see both heated phonons in the same spectrum (see text).

corrected for the instrumental bandwidths as done earlier in Sec. V A.

A large heating of the 2ω phonons is not unexpected. Based on the results of the Appendix and on the experimental coupling constants G_{ij},[24,25] one finds the coupling strengths for the ST and L modes to their respective $\Delta m_s = 1$ and $\Delta m_s = 2$ transitions to be comparable. The width of the $\Delta m_s = 2$ spin resonance,[37] however, will be considerably less than that of the strain-broadened $\Delta m_s = 1$ resonance since the $\Delta m_s = 2$ level splitting is unaffected (to first order in perturbation theory) by local lattice strains. The generated 2ω phonons are, therefore, confined to a smaller energy interval than the ω phonons and a far greater true effective phonon temperature is anticipated.

A direct measurement of the 2ω-phonon linewidth using the movable-aperture technique described in an earlier section was difficult because of the two-mirror system incorporated into the experimental arrangement. However, in an attempt to obtain some qualitative information about the characteristics of these 2ω phonons, we have undertaken the following experiment: Beginning with the klystron frequency and applied magnetic field tuned for maximum ω-phonon heating at the center of the $\Delta m_s = 1$ resonance line, we have varied the klystron frequency and magnetic field in order to saturate different portions of the $\Delta m_s = 1$ resonance and have observed the resultant phonon heating at ω and 2ω. (Because of the strong resonance absorption of the MgO:Ni^{2+} samples, the loaded-cavity resonant frequency is a sensitive function of applied magnetic field strength; thus, for various choices of the klystron frequency and the magnetic field, one can selectively perturb different points in the $\Delta m_s = 1$ resonance line. However, due to the nonlinear nature of the cavity-pulling effects, this procedure does not permit a determination of the exact portion of the resonance undergoing cw saturation in our experiment.) Starting at a point where the ω-phonon scattering intensity is a maximum, the data show the 2ω-phonon scattering intensity to increase rapidly by a factor of 5 with a klystron frequency change of ~20 MHz and then to drop off rapidly again with further changes in frequency; by contrast, the ω-phonon heating decreases quickly with a change in frequency from its peak intensity at line center to a lower, less frequency-dependent value as described earlier in Sec. V A.

Although a quantitative interpretation of the phonon behaviors is difficult without knowing the exact point in the resonance undergoing saturation, several aspects of the heating are noteworthy. The narrow frequency interval of 2ω-phonon heating, as compared to the rather extended region of uniform ω-phonon heating (neglecting, for the moment, the behavior at line center), is very suggestive of a 2ω-phonon bandwidth significantly less than that for the ω phonons. Such behavior is consistent with our earlier predictions of a small 2ω-phonon bandwidth, which results from the easy exchange of energy between spin levels and strong double-quantum transitions at line center and from the insensitivity of the $\Delta m_s = 2$ level splitting to local lattice strains.

Quite unexpected, however, is the observation that the heatings of ω and 2ω phonons maximize with microwave saturation of *different* portions of the $\Delta m_s = 1$ resonance. This is in direct contradiction to the predictions of the rate-equation formalism presented here and in DBSS,[14] which indicate maximum heating for both phonons with saturation of the resonance at line center. The reason for the discrepancy is not known, although several possible explanations appear plausible. For example, the theoretical analysis of the $S = 1$ system completely neglects the effect of double-quantum transitions involving microwave photons and/or phonons on the resonant phonon heating. The work of Shiren[38] on the double-quantum effect in MgO:Ni^{2+} and MgO:Fe^{2+} is of particular interest; he shows that the phonon-photon transition probability between the $S_z = \pm 1$ levels may be comparable to or greater than the single 2ω-phonon transition probability under suitable conditions. The presence of a strong microwave saturating field and large ω-phonon excitations may, therefore, selectively enhance the ω-phonon heating at the expense of the 2ω-phonon excitation and could explain the rapid variations in phonon excitations very near to line center where the double-quantum effect is strongest.

Also, when the excitations of the ω and 2ω phonons become large, the breakup of 2ω phonons into pairs of ω phonons due to three-phonon anharmonic processes can become significant. Theoretical considerations[30,39] show that, in particular, a longitudinal phonon at 2ω will typically split into a pair of transverse phonons at $\sim\omega$ or a longitudinal and transverse phonon, each at $\sim\omega$, and that this 2ω-phonon breakup becomes more pronounced the greater the effective temperatures of the phonons involved. The observed reduction of the 2ω-phonon excitation and the enhancement of the ω-phonon heating at line center may possibly result from such a process; further indication of such a possible breakup in the 2ω phonons is given in Sec. V G, where the anomalously high heating of ST phonons is suggested to arise from a parametric process in which 2ω phonons are down-converted into ω phonons.

The appearance of the forbidden L phonons at ω as described in Sec. V E may also be due, in part, to the breakup of 2ω longitudinal phonons generated by the allowed $\Delta S_z = -2$ transition. However, this

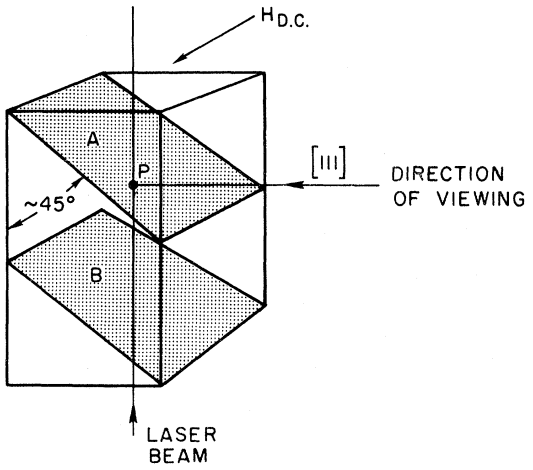

FIG. 18. Illustrating planes A and B in crystal in which anomalously intense phonon heating was found. The scattering point labeled P was varied by moving the Dewar holding the crystal and by displacing the laser beam, while keeping the collection optics fixed.

seems unlikely as the L phonons at frequency ω generated in this fashion would be expected to have the same sharp tuning characteristics as the 2ω phonons and no such behavior was observed for the L phonons shown in Fig. 14(b).

G. Anomalously High Phonon Heating

In this section we further emphasize the unique selectivity of Brillouin scattering as a probe of phonon heating by discussing (a) the spatial probing of the heating, (b) a large asymmetry in the heating of Stokes and anti-Stokes lines of the same phonon in certain regions of the crystal, and (c) a suggested phonon parametric amplification.

As pointed out earlier, the phonons are probed at a "point" in the crystal determined by the intersection of the laser beam and the axis of the optical detection system, as shown in Fig. 6. By a combination of movements of the laser beam and the crystal (the latter achieved by moving the Dewar), different points in the crystal may be probed. The data which have been presented so far were taken in a region which was near the center of the sample. In probing away from the center of the sample, selected planes were discovered in which the phonon heating in either the Stokes or anti-Stokes line (but not both) reaches extraordinarily high effective temperatures, i.e., as high as 40 000 °K. This anomalous heating was found in planes A and B as shown in Fig. 18. These planes intersected the crystal edges and made an angle of approximately 45° with the vertical as shown. It was difficult to specify precisely the thickness of the planes but it was approximately 0.5 mm. The heating was not completely uniform in the plane and was somewhat stronger towards the edges. The observed anomalous heating was also very asymmetric between Stokes and anti-Stokes lines, and, moreover, the asymmetry was *reversed* between planes A and B as shown in Fig. 19. A preliminary measure of the degree of heating being observed here may be had by noting that the peak counts at room temperature for the same integration time of 40 sec were 3000. To get the effective temperature of these hot phonons, their bandwidth must first be determined by angular scanning, as outlined earlier, and compared with the 900-MHz-bandwidth room-temperature thermal phonons accepted by the collecting lens. A typical angular

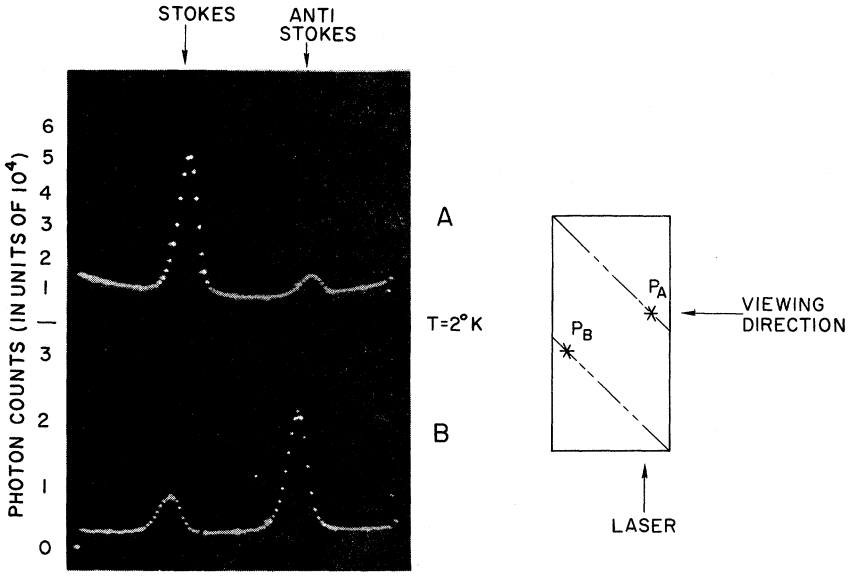

FIG. 19. Brillouin scattering at 2 °K from resonantly heated slow-transverse phonons at 25.6 GHz (labeled $\tilde{q}_A$ in Fig. 4) at points P_A and P_B in planes A and B (shown in Fig. 18), respectively, in sample MS-4A. Note the large asymmetry between Stokes and anti-Stokes phonons and reversal of this asymmetry from A to B. The gain in B has been increased by a factor of 2. The degree of heating shown for the anti-Stokes in A and the Stokes in B roughly corresponds to that described earlier for MS-4A in other regions of the crystal outside these planes. In contrast, the heating of the Stokes in A is anomalously high, i.e., an order of magnitude larger.

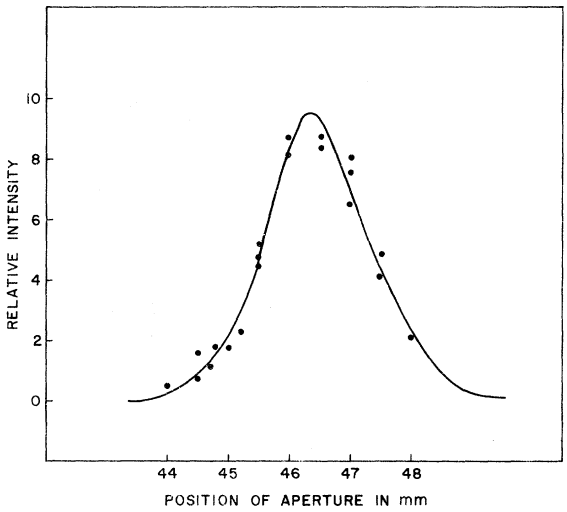

FIG. 20. Determination of frequency bandwidth of anomalously hot phonons in planes A and B by measuring angular aperture of Brillouin-scattered light using method depicted in Fig. 6. 1-mm displacement in aperture position is equivalent to 40 MHz of bandwidth, so that anomalously hot phonons have a bandwidth of ~ 80 MHz. This implies an effective temperature for the Stokes phonons at point A of $\sim 40\,000$ °K (see text).

scan of these anomalously hot phonons is shown in Fig. 20. A 0.5-mm aperture was used and here again 1 mm in scanning distance corresponds to 40 MHz, so that the bandwidth of these hot phonons is less than 80 MHz. Thus, the effective temperature of the Stokes line at point A which shows 42×10^3 peak counts would be $T_{eff} \simeq (42\times10^3/3\times10^3) \times \frac{900}{80} \times 273$ °K $= 42\,500$ °K! This intense heating, in addition to being observed in the indicated planes, was only observed when the dc magnetic field was sharply tuned to line center. It is of course at line center that the double-quantum transition is most effective in saturating the entire inhomogeneous line even without the aid of spin diffusion.

This intense heating has all the earmarks of a threshold and nonlinear phenomenon. For example, it is very sensitive to the field being at line center, as just cited, in contrast to the normal heating which is quite effective over the entire Ni^{2+} EPR linewidth. Of course, increased heating which tunes very sharply with field at line center is observed throughout the crystal; however, in contrast to the phonon excitation in planes A and B, the increased heating elsewhere was only a factor of 2 greater as discussed earlier. In addition, the anomalously high heating seems to be microwave-power dependent in a nonlinear fashion, although this latter point was difficult to check in a precise quantitative way due to the dispersive properties of the specimen-vs-microwave-power level. Moreover, it was found that surface contamination of the specimen (by the cement used to hold the specimen, for example) would destroy this anomalously large heating. Upon cleaning the surface, the intense heating could be restored. This is suggestive of a threshold value of the acoustic Q of some mode in the sample for the onset of some parametric process. Without going into details, which will be presented in a later publication, we would like to suggest that this anomalously high heating is due to a parametric process in which the 2ω phonons are down-converted into ω phonons. The 2ω phonons are very sharp, corresponding to the $m_s = +1$ to $m_s = -1$ transition and, given the acoustic nonlinearity of MgO, a threshold will exist for the down-conversion of the 2ω phonons into ω phonons when interacting with phonons in the vicinity of ω. This type of unstable phonon breakdown has been seen in the rf range.[40]

A major unanswered question is the origin of the asymmetry between Stokes and anti-Stokes lines when this intense heating is observed, as well as its reversal between planes. Since the difference between Stokes and anti-Stokes components is that between phonons traveling away from or towards the direction of viewing, the reversal of intensity between points A and B is consistent with the hot phonons traveling *towards* the corners of the crystals. The exact significance of travel towards the corner in increasing the intensity is not clear. We are currently considering different phonon-focusing mechanisms which would concentrate the energy generated by the spin system in one direction as compared to the reverse for particular cavity modes. That the corners are playing some role is evidenced by the fact that the beveled crystal shown in Fig. 13 used to study the 25-GHz L phonons showed only a very small anomaly. In concluding this section, we cite the above observations, although some remain as puzzles, as an indication of the diverse and rich phenomena in the phonon bottleneck that can only be probed by Brillouin light scattering.

VI. CONCLUSIONS

We have described the observation of nonequilibrium phonons due to a microwave-phonon bottleneck in Ni^{2+}:MgO by Brillouin light scattering. The bandwidth of the heated phonons was found to be less than the EPR linewidth. In addition, the bottleneck was observed to persist up to crystal temperatures as high as 40 °K in accord with the fact that τ_{ph} below this temperature is not due to intrinsic temperature-dependent anharmonic processes but is determined by crystal geometry and surface condition. Phonon-lifetime measurements are in accord with this fact and evidence from Brillouin light scattering has also been presented to indicate a certain degree of phonon-mode conversion. Gen-

eration of 2ω phonons by the $S=1$ spin system has also been observed, as well as anomalously high heating of the ω phonons in some regions of the crystal under certain conditions ascribed to a parametric process involving the 2ω phonons.

While many aspects of the phonon bottleneck have been verified and fit the simple accepted theory, many questions are suggested by our results but remain unanswered. The whole question of phonon loss out of the crystal and mode conversion at these frequencies needs further study. The observation of the reflection from a crystal boundary of an incident transverse wave (generated by standard pulsed-microwave acoustic techniques) by means of Brillouin light scattering should prove very helpful in answering this question. A study of the heating and decay of still other phonons at the same frequency but traveling in different directions should also help clarify the role of mode conversion; a more detailed study of geometrical factors and surface preparation is also called for, especially in connection with the anomalous phonon heating described in Sec. V G. In all, it becomes apparent that Brillouin light scattering should be able to play an important role in clarifying many of the remaining questions connected with the microwave-phonon bottleneck.

ACKNOWLEDGMENTS

We wish to thank the following for their help: E. I. Gordon, J. J. Parker, and A. M. Johnson for supplying many of the laser components and advice regarding its construction; A. L. Albert, W. Gronros, and L. B. Hooker for sample preparation; D. L. Wood and B. Prescott for measuring the Ni^{2+} concentration in our samples; W. Mims and L. R. Walker for many helpful discussions; and B. Chambers and R. Fulton for their aid in computations.

APPENDIX: SPIN-PHONON-COUPLING SELECTION RULES

It is most convenient to describe the interaction of the phonons with the spins by a phenomenological perturbation Hamiltonian or dynamic spin Hamiltonian of the form[34,41-44]

$$\mathcal{H}' = \mu_B \vec{H} \cdot \overleftrightarrow{\delta g} \cdot \vec{S} + \vec{S} \cdot \overleftrightarrow{\delta D} \cdot \vec{S}, \tag{A1}$$

where hyperfine field terms have been omitted. $\overleftrightarrow{\delta g}$ and $\overleftrightarrow{\delta D}$ are second-rank tensors which depend linearly on the strain and are written[25,34,44]

$$\delta g_{ij} = \sum_{kl} G'_{ijkl} e_{kl} \tag{A2a}$$

and

$$\delta D_{ij} = \sum_{kl} G_{ijkl} e_{kl}, \tag{A2b}$$

where e_{kl} are the strains

$$e_{kl} = \frac{1}{2}\left(\frac{\partial u_k}{\partial x_l} + \frac{\partial u_l}{\partial x_k}\right). \tag{A3}$$

Equations (A1) and (A2) are appropriate to either a static strain produced by external stress or a time-varying strain produced by the phonons (in the long-wavelength approximation such that the local strains are the same whether produced by external stress or the phonons so that the elements of the G tensor may be measured by application of external stress). For ions such as Ni^{2+} whose cubic crystalline field ground states are orbital singlets, the ratio of the Zeeman term in (A1) to the term quadratic in the spin operators will be of the order of $\mu_B H/\lambda$, i.e., the Zeeman energy/spin-orbit coupling. This is so since the terms linear in S arise from perturbation terms of the type $\langle 0|\lambda \vec{L}\cdot\vec{S}|e\rangle\langle e|\mu_B \vec{H}\cdot\vec{L}|0\rangle$, whereas the terms quadratic in S arise from terms of the form $\langle 0|\lambda \vec{L}\cdot\vec{S}|e\rangle\langle e|\lambda \vec{L}\cdot\vec{S}|0\rangle$, where $|e\rangle$ is an excited orbital state and $|0\rangle$ is the ground state. Thus, the terms linear in S are negligible compared to the D terms, except for $S=\frac{1}{2}$, in which case the D term vanishes. (S may be a fictitious spin.)

The fourth-rank tensor G simplifies in the case of cubic symmetry and only two constants are needed; $-\mathcal{H}'$ then may be written in irreducible tensor notation as [42-44]

$$\begin{aligned}\mathcal{H}' = {} & G_{11}\left[\tfrac{1}{2}(2S_z^2 - S_x^2 - S_y^2)\,\tfrac{1}{2}(2e_{zz} - e_{xx} - e_{yy})\right. \\ & \left. + \tfrac{1}{2}\sqrt{3}\,(S_x^2 - S_y^2)\,\tfrac{1}{2}\sqrt{3}\,(e_{xx} - e_{yy})\right] \\ & + G_{44}\begin{Bmatrix} (S_y S_z + S_z S_y)\, e_{yz} \\ + (S_z S_x + S_x S_z)\, e_{zx} \\ + (S_x S_y + S_y S_x)\, e_{xy} \end{Bmatrix},\end{aligned} \tag{A4}$$

where x, y, z are the cubic axes.

The spin operators and corresponding strain expressions associated with G_{11} transform as the θ, e bases of the Γ_3 cubic representation, whereas those appearing with G_{44} transform as Γ_5. The strains in (A4) produced by the phonons may be expressed in terms of the direction of propagation $\vec{\lambda}$ and the polarization $\vec{\varphi}$ of the phonons so that, for example, $e_{yz} \to (\varphi_y \lambda_z + \varphi_z \lambda_y)e$, where e is the magnitude of the strain.

Expression (A4) is in convenient form for the case of the external magnetic field along any of the cube axes. In our experiment the magnetic field H_0 was applied along a cube face diagonal which we take to be a [101] direction; we choose this direction of the applied field as the new z' axis and the new y' axis to correspond with the old y axis. (Our results are applicable to all equivalent [101] directions, providing the x', y', and z' axes are appropriately defined.) With this new choice of axes the terms in the Hamiltonian containing the spin operators transform as follows:

$$\mathcal{H}_2 = \tfrac{1}{2}(2S_z^2 - S_x^2 - S_y^2) = \tfrac{1}{2}[\tfrac{1}{2}(S_{z'}^2 + S_{x'}^2) - \tfrac{3}{2}(S_{z'}S_{x'} + S_{x'}S_{z'}) - S_{y'}^2],$$

$$\mathcal{H}_3 = \tfrac{1}{2}\sqrt{3}(S_x^2 - S_y^2) = \tfrac{1}{2}\sqrt{3}[\tfrac{1}{2}(S_{x'}^2 + S_{z'}^2) + \tfrac{1}{2}(S_{z'}S_{x'} + S_{x'}S_{z'}) - S_{y'}^2],$$

$$\mathcal{H}_4 = (S_y S_z + S_z S_y) = \tfrac{1}{2}\sqrt{2}(S_{y'}S_{z'} - S_{y'}S_{x'} + S_{z'}S_{y'} - S_{x'}S_{y'}), \tag{A5}$$

$$\mathcal{H}_5 = (S_z S_x + S_x S_z) = (S_{z'}^2 - S_{x'}^2),$$

$$\mathcal{H}_6 = (S_x S_y + S_y S_x) = \tfrac{1}{2}\sqrt{2}(S_{x'}S_{y'} + S_{z'}S_{y'} + S_{y'}S_{x'} + S_{y'}S_{z'});$$

$$a_2 = \tfrac{1}{2}(2\lambda_z\varphi_z - \lambda_x\varphi_x - \lambda_y\varphi_y) = \tfrac{1}{2}[\tfrac{1}{2}(\lambda_{z'}\varphi_{z'} + \lambda_{x'}\varphi_{x'}) - \tfrac{3}{2}(\lambda_{z'}\varphi_{x'} + \lambda_{x'}\varphi_{z'}) - \lambda_{y'}\varphi_{y'}],$$

$$a_3 = \tfrac{1}{2}\sqrt{3}(\lambda_x\varphi_x - \lambda_y\varphi_y) = \tfrac{1}{2}\sqrt{3}[\tfrac{1}{2}(\lambda_{x'}\varphi_{x'} + \lambda_{z'}\varphi_{z'}) + \tfrac{1}{2}(\lambda_{z'}\varphi_{x'} + \lambda_{x'}\varphi_{z'}) - \lambda_{y'}\varphi_{y'}].$$

$$a_4 = (\lambda_y\varphi_z + \lambda_z\varphi_y) = \tfrac{1}{2}\sqrt{2}(\lambda_{y'}\varphi_{z'} - \lambda_{y'}\varphi_{x'} + \lambda_{z'}\varphi_{y'} - \lambda_{x'}\varphi_{y'}), \tag{A6}$$

$$a_5 = (\lambda_z\varphi_x + \lambda_x\varphi_z) = (\lambda_{z'}\varphi_{z'} - \lambda_{x'}\varphi_{x'}),$$

$$a_6 = (\lambda_x\varphi_y + \lambda_y\varphi_x) = \tfrac{1}{2}\sqrt{2}(\lambda_{x'}\varphi_{y'} + \lambda_{z'}\varphi_{y'} + \lambda_{y'}\varphi_{z'}).$$

As our light-scattering plane is a $(1\bar{1}0)$ plane, we are only interested in phonons traveling in this plane, i.e., $\lambda_{z'} = 0$. Phonons traveling in this principal plane are either polarized perpendicular to the plane or parallel to the plane.

Case I. Phonons traveling in $(1\bar{1}0)$ *plane and polarized perpendicular to the plane.* In this case $\varphi_{x'} = \varphi_{y'} = 0$ and $\varphi_{z'} = 1$. Our a's now become

$$a_2 = -\tfrac{3}{4}\lambda_{x'}, \quad a_3 = \tfrac{1}{4}\sqrt{3}\lambda_{x'}, \quad a_4 = \tfrac{1}{2}\sqrt{2}\lambda_{y'}, \quad a_5 = 0, \quad a_6 = \tfrac{1}{2}\sqrt{2}\lambda_{y'}. \tag{A7}$$

The Hamiltonian in this case becomes

$$\mathcal{H}' = \tfrac{3}{4}G_{11}\lambda_{x'}(S_{z'}S_{x'} + S_{x'}S_{z'})e + G_{44}\lambda_{y'}(S_{z'}S_{y'} + S_{y'}S_{z'})e, \tag{A8}$$

which will induce only $\Delta m_s = \pm 1$ transitions. Since experimentally it is found[24,25] that $G_{11} \approx \frac{3}{2}G_{44}$, we see that the coupling to these $\Delta m_s = 1$ phonons will be essentially uniform for all directions in this plane, neglecting the $1/v^2$ variation due to the cubic anisotropy of the sound velocity.

Case II. Phonons traveling in $(1\bar{1}0)$ *plane and polarized in this plane,* $\lambda_{z'} = 0$, $\varphi_{z'} = 0$. These will be longitudinal and transverse phonons (but of course are only pure along principal directions). We will demonstrate that there are no $\Delta m_s = 1$ transitions in this case so that only 2ω phonons are launched into this plane by the relaxing spins.

With $\lambda_{z'} = 0$ and $\varphi_{z'} = 0$, we have

$$a_2 = \tfrac{1}{4}\lambda_{x'}\varphi_{x'} - \tfrac{1}{2}\lambda_{y'}\varphi_{y'},$$

$$a_3 = \tfrac{1}{4}\sqrt{3}\lambda_{x'}\varphi_{x'} - \tfrac{1}{2}\sqrt{3}\lambda_{y'}\varphi_{y'}, \tag{A9}$$

$$a_4 = -\tfrac{1}{2}\sqrt{2}(\lambda_{x'}\varphi_{y'} + \lambda_{y'}\varphi_{x'}),$$

$$a_5 = -\lambda_{x'}\varphi_{x'}, \quad a_6 = \tfrac{1}{2}\sqrt{2}(\lambda_{x'}\varphi_{y'} + \lambda_{y'}\varphi_{x'}).$$

Our spin-phonon Hamiltonian now becomes

$$\mathcal{H}' = G_{11}(\tfrac{1}{4}\lambda_{x'}\varphi_{x'} - \tfrac{1}{2}\lambda_{y'}\varphi_{y'})(S_{z'}^2 + S_{x'}^2 - 2S_{y'}^2)e + G_{44}[(\lambda_{x'}\varphi_{y'} + \lambda_{y'}\varphi_{x'})(1/2i)(S_+^2 - S_-^2) - \lambda_{x'}\varphi_{x'}(S_{z'}^2 - S_{x'}^2)]e. \tag{A10}$$

It is apparent that the spin operators in Eq. (A10) induce only $\Delta m_s = 2$ transitions. Thus, the spins cannot generate longitudinal phonons at frequency ω corresponding to $\Delta m_s = 1$.

It is helpful to have a geometric visualization of these selection rules. For example, in Fig. 21(a), we show the local movement of ions for a phonon traveling perpendicular to H_0 and whose polarization is also perpendicular to H_0. In Fig. 21(a) it is shown as a longitudinal wave and the transverse wave would simply have the polarization vectors rotated 90°. The O^{2-} ions lying directly above and below the Ni^{2+} have no displacement relative to the Ni^{2+} ion. In Fig. 21(b) is shown the equivalent local distortion as viewed from the central Ni^{2+} ion, and it is immediately seen that this corresponds

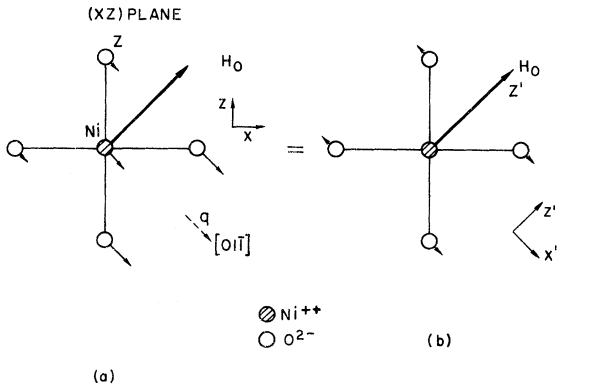

FIG. 21. Visualization of spin-phonon selection rules. (a) Displacement of ions in neighborhood of Ni^{2+} due to longitudinal phonon traveling in $[10\bar{1}]$ direction. O^{2-} ions immediately above and below Ni^{2+} are displaced by same amount and in same direction as Ni^{2+}. (b) Equivalent displacements as viewed from Ni^{2+} ion, giving rise to D and E terms relative to H_0 or $\Delta m_s = 2$ transitions only.

to the addition of a term $E(S_{x'}^2 - S_{y'}^2) + DS_{z'}^2$ to the erstwhile cubic Hamiltonian with z' along H_0. The inclusion of the motion of other than near-neighbor ions is easily seen to preserve the symmetry of the local distortion so that only D and E terms relative to H_0 are involved, giving rise only to $\Delta m_s = 2$ transitions. The other selection rules discussed above can be similarly visualized.

---

*Present address: Sandia Laboratories, Albuquerque, N. M. Part of the analytical work and preparation of this manuscript was performed by one of the authors (W. J. B.) at Sandia Laboratories.

[1]J. H. Van Vleck, Phys. Rev. 59, 724 (1941).

[2]P. L. Scott and C. D. Jeffries, Phys. Rev. 127, 32 (1962).

[3]J. A. Giordmaine, L. E. Alsop, F. R. Nash, and C. H. Townes, Phys. Rev. 109, 302 (1958); J. A. Giordmaine and F. R. Nash, *ibid.* 138, A1510 (1965).

[4]B. W. Faughnan and M. W. P. Strandberg, J. Phys. Chem. Solids 19, 155 (1961).

[5]W. J. Brya and P. E. Wagner, Phys. Rev. Letters 14, 431 (1965); Phys. Rev. 157, 400 (1967).

[6]W. B. Mims and D. R. Taylor, Phys. Rev. Letters 22, 1430 (1969); Phys. Rev. B 3, 2103 (1971).

[7]N. S. Shiren, Phys. Rev. Letters 17, 958 (1966); in *Proceedings of the XIVth Colloque Ampere, Ljubljana,* 1966 (North-Holland, Amsterdam, 1967).

[8]C. H. Anderson and E. S. Sabisky, Phys. Rev. Letters 21, 987 (1968).

[9]S. S. Rifman and P. E. Wagner, Solid State Commun. 7, 453 (1969).

[10]Professor A. Kastler has kindly called to our attention a section of a paper written by him in 1952 in which the possibility of seeing the microwave-phonon bottleneck by Brillouin scattering is suggested [A. Kastler, Experientia 8, 1 (1952)]. The experimental techniques available then, however, would have rendered such an experiment many orders of magnitude more diffucult. From a practical point of view, it was the advent of high-intensity monochromatic laser sources and improvement in photon-processing equipment which made this experiment feasible.

[11]W. J. Brya, S. Geschwind, and G. E. Devlin, Phys. Rev. Letters 21, 1800 (1968).

[12]S. A. Al'tshuler, R. M. Valishev, and A. Kh. Khasanov, Zh. Eksperim. i Teor. Fiz. Pis'ma v Redaktsiyu 10, 179 (1969) [Sov. Phys. JETP Letters 10, 113 (1969)]; R. M. Valishev and A. Kh. Khasanov, Fiz. Tverd. Tela 12, 3521 (1970) [Sov. Phys. Solid State 12, 2859 (1971)]; S. A. Al'tshuler, R. M. Valishev, B. I. Kochelaev, and A. Kh. Khasanov, Zh. Eksperim. i Teor. Fiz. Pis'ma v Redaktsiyu 13, 535 (1971) [Sov. Phys. JETP Letters 13, 382 (1971)].

[13]S. Geschwind and G. Devlin (unpublished).

[14]W. J. Brya, Phys. Rev. B 3, 635 (1971).

[15]Excellent accounts of the Brillouin-scattering formalism are given by I. L. Fabelinskii, *Molecular Scattering of Light* (Plenum, New York, 1968); and G. B. Benedek and K. Fritsch, Phys. Rev. 149, 647 (1966).

[16]The expression for $\vec{\zeta}_\mu$ as given by Benedek and Fritsch (Ref. 15) seems to define p_{44} in such a fashion as to be a factor of 2 larger than that given by us in Eq. (19b). Our modification of their expression, which is consistent with the usual definition for the elasto-optic constants [J. F. Nye, *Physical Properties of Crystals* (Oxford U. P., London, 1957)], is obtained by replacing their p_{44} with the quantity $2p_{44}$.

[17]R. F. S. Hearmon, in *Landolt-Börnstein Tables, New Series,* Vol. III/1 (Springer-Verlag, New York, 1966), p. 8.

[18]R. Bechmann, in Ref. 17, p. 138.

[19]A. E. H. Love, *Theory of Elasticity*, 4th ed. (Cambridge U. P., New York, 1934), p. 298.

[20]W. Low, Phys. Rev. 109, 247 (1958).

[21]S. Koritnig, in *Landolt-Börnstein Tables*, 6th ed., Vol. II/8 (Springer-Verlag, Berlin, 1962), p. 64.

[22]Designed by M. B. Graifman of Bell Telephone Laboratories. A schematic representation of the system is given by P. A. Fleury and R. Loudon, Phys. Rev. 166, 514 (1968).

[23]Designed and manufactured by L. F. Mollenauer and C. D. Grandt.

[24]N. S. Shiren, Bull. Am. Phys. Soc. 7, 29 (1962).

[25]G. D. Watkins and E. R. Feher, Bull. Am. Phys. Soc. 7, 29 (1962); E. Feher, Phys. Rev. 136, A145 (1964).

[26]M. F. Lewis and A. M. Stoneham, Phys. Rev. 164, 271 (1967).

[27]C. H. Anderson and E. S. Sabisky, in *Physical Acoustics*, edited by W. P. Mason and R. N. Thurston (Academic, New York, 1971), Vol. 8, Chap. 1.

[28]J. Wilks, *The Properties of Liquid and Solid He* (Oxford U. P., London, 1967), p. 422ff.

[29]M. Pomerantz, Phys. Rev. 139, A501 (1965).

[30]L. Landau and G. Rumer, Physik. Z. Sowjetunion 11, 18 (1937).

[31]V. Narayanamurti and M. Chin (private communication).

[32]G. Devlin, J. Davis, L. Chase, and S. Geschwind, Appl. Phys. Letters 19, 138 (1971).

[33]P. L. Donoho, Phys. Rev. 133, A1080 (1964); R. B. Hemphill, P. L. Donoho, and E. D. McDonald, *ibid.* 146, 329 (1966).

[34]S. A. Marshall, T. T. Kikuchi, and A. R. Reinberg, Phys. Rev. 125, 453 (1962); P. R. Locher and S. Geschwind, Phys. Rev. Letters 11, 333 (1963).

[35]The apparent breakdown of spin-phonon selection rules is also familiar in standard microwave acoustic experiments and has similarly been ascribed to mode conversion of the primary phonons launched by the transducer due to boundary reflections. See E. B. Tucker, Proc. IEEE 53, 1547 (1965) and the discussion on p. 1559 of this reference.

[36]A. Sommerfeld, *Mechanics of Deformable Bodies* (Academic, New York, 1964).

[37]S. R. P. Smith, F. Dravnieks, and J. E. Wertz, Phys. Rev. 178, 471 (1969).

[38]N. S. Shiren, Phys. Rev. Letters 6, 168 (1961); Appl. Phys. Letters 7, 142 (1965); *Physics of Quantum Electronics* (McGraw-Hill, New York, 1966), p. 385.

[39]R. Orbach and L. A. Vredevoe, Physics 1, 91 (1964).

[40]M. Lukkala, Phys. Status Solidi 29, 377 (1968); Ann. Acad. Sci Fennicae Ser. A VI Physica No. 306 (1969); Phys. Letters 25A, 76 (1967).

[41]J. H. Van Vleck, Phys. Rev. 57, 426 (1940).

[42]E. B. Tucker, Proc. IEEE 53, 1547 (1965).

[43]S. A. Al'tshuler, B. I. Kochelaev, and A. M. Leushin, Usp. Fiz. Nauk 75, 459 (1961) [Sov. Phys. Usp.

4, 880 (1962)]. Our e_{ij}'s are the strain elements and should not be confused with the ϵ's in this reference which are related to our G's; i.e., Tucker (Ref. 42) gives the correspondence $G_{11}=\frac{4}{3}\epsilon_2 R$, $G_{44}=\epsilon_5 R$.

[44]R. D. Mattuck and M. W. P. Strandberg, Phys. Rev. 119, 1204 (1960).

PHYSICAL REVIEW B VOLUME 6, NUMBER 5 1 SEPTEMBER 1972

Neutron-Scattering Study of the Ferroelectric Phase Transformation in $Tb_2(MoO_4)_3$ †

B. Dorner,* J. D. Axe, and G. Shirane
Brookhaven National Laboratory, Upton, New York 11973
(Received 24 April 1972)

We establish a first example of a ferroelectric phase transformation where a Brillouin-zone-boundary soft mode [at the M point $(\frac{1}{2},\frac{1}{2},0)$] rather than a Brillouin-zone-center mode of the parent paraelectric phase (PE) is responsible for the transition. By inelastic scattering of neutrons, we have measured low-frequency phonon-dispersion relations in $Tb_2(MoO_4)_3$ for symmetry directions emanating from the M point in PE. For $T > T_0 = 159\,°C$ the frequency ω_M of a doubly degenerate mode at M follows a Curie-Weiss law $\omega_M^2 = A(T - T_C)$, with $A = 0.0165$ meV^2/°C and $T_C = 149\,°C$. With the help of group theory, the symmetry properties of soft modes which lead from the PE symmetry (tetragonal $P\bar{4}2_1m$) to the symmetry (orthorhombic $Pba2$) of the ferroelectric (FE) phase were determined. The soft-mode eigenvectors contain parameters which are not fixed by symmetry and their "static" values can be obtained from existing x-ray–structure data. "Dynamic" values are determined here from the integrated inelastic-scattering intensity of the soft mode measured in PE at various M points. The "static" and the "dynamic" values are in good agreement. The condensation of such an antiferroelectric soft mode cannot directly produce the spontaneous polarization P_z in FE. As has been suggested theoretically, our measurements show that the antiferroelectric static displacements constitute the order parameter, which couples to a shear strain u_{xy}, which in turn produces the polarization by piezoelectric coupling. The spontaneous polarization and the spontaneous strain in FE are shown to be proportional to the square of this order parameter. From the initial slopes of acoustic branches we derive a set of elastic constants in PE.

I. INTRODUCTION

Several rare-earth molybdates were discovered by Borchardt and Bierstedt[1] to undergo ferroelectric phase transformations at transition temperatures $150 < T < 190\,°C$. These materials[2,3] show many unusual properties. In a stress-free crystal, a small dielectric anomaly is found at low frequencies in the ferroelectric phase (FE). In the high-temperature paraelectric phase (PE) the dielectric constant is independent of temperature. On the other hand, the clamped crystal does not show a dielectric anomaly at all.[4] Similarly, the elastic properties show an anomaly below the transition only.[4,5] Coupled with spontaneous polarization states of opposite polarity ($\pm P_z$, which of course can be switched by an applied electric field)[6] are two mechanical configurations described by a shear strain $\pm u_{xy}$ (see Fig. 1). One mechanical configuration can be switched into another by an applied mechanical stress.[7] This has been described as ferroelastic behavior.[8] But ferroelectricity and ferroelasticity in this material are so coupled that P_z and u_{xy} change simultaneously.

The coupling of elastic and dielectric properties, together with the absence of a dielectric anomaly in the clamped crystal, led Cross *et al.*[4] to the conclusion that the spontaneous polarization was an incidental but necessary consequence of the strain u_{xy}, since the piezoelectric constant a_{36} (coordinates of PE) is nonzero.[5,9] Pytte,[10] however, suggested that this picture was incomplete and that the transition is fundamentally connected with a doubly degenerate soft mode at the Brillouin-zone edge in PE, which leads to a doubling of the unit cell. Independently, Levanyuk and Sannikov[11] and Aizu[12] came to the same conclusion.

The only experimental technique capable of direct investigation of such a proposed mechanism is that of inelastic neutron scattering. This paper presents such a study. A preliminary account of this work has already been reported.[13] When this work was begun, some uncertainty existed in the literature concerning the sizes of the PE and FE unit cells. In preliminary experiments, we therefore established that the anticipated doubling of the cell volume does in fact occur. Subsequently reliable structure determinations in the FE phase of isostructural $Gd_2(MoO_4)_3$ (GMO) by Keve *et al.*[14] and in both phases by Jeitschko[15] have been reported. The recent data are in substantial agreement with those given in Table I for $Tb_2(MoO_4)_3$ (TMO).[16–18]

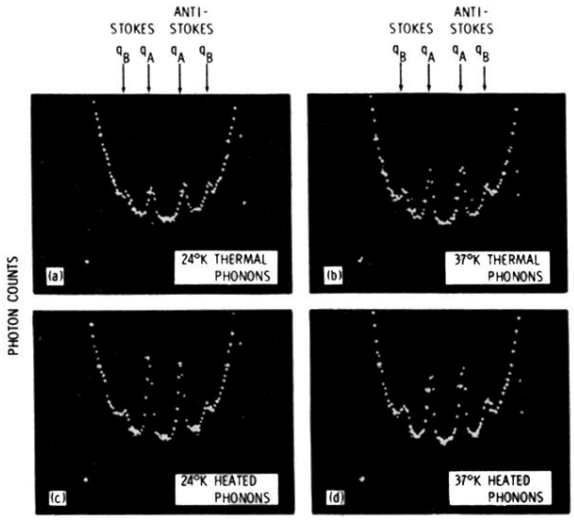

FIG. 11. Brillouin-scattered light from microwave-phonon bottleneck at elevated temperature, corresponding to same configuration shown in Fig. 4. Frequencies of $\tilde{q}_A$ and $\tilde{q}_B$ are the same as in Fig. 4. (a) and (b) show thermal scattering with microwaves off while (c) and (d) show the heated phonons $\tilde{q}_A$ at 25.6 GHz when the saturating microwaves are on.

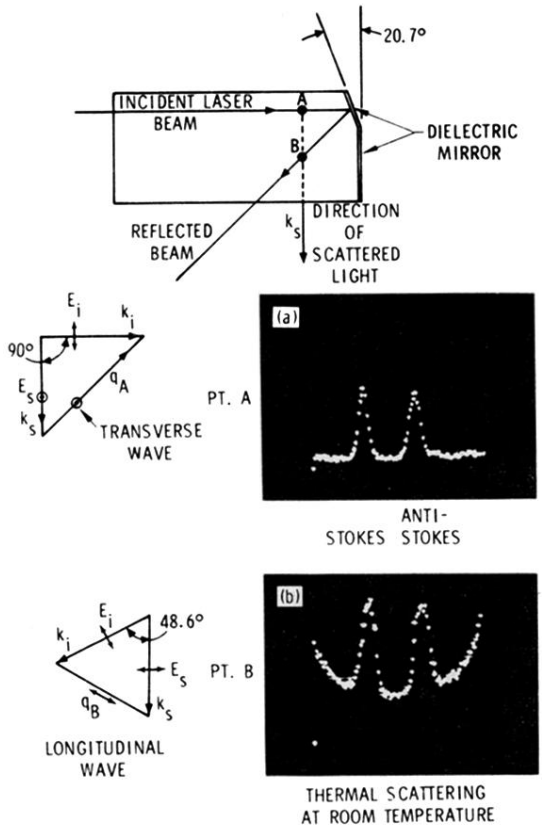

FIG. 13. Configuration of 1% Ni^{2+}:MgO crystal used to observe simultaneously 25.6-GHz ST and L phonons. Scattering triangle for incident laser beam is shown to left of (a) and selects a value of $\vec{q}$ which corresponds to 25.6-GHz ST phonons. Appropriate scattering diagram for reflected laser beam is to left of (b) and corresponds to a shallower scattering angle and smaller $\vec{q}$, such that the longitudinal phonons at this reduced $\vec{q}$ are also at 25.6GHz. Polarizations of scattered light in (a) and (b) are at right angles to each other so that one may view either transverse phonons at point *A* or longitudinal phonons at point *B* by 90° rotation of polarizer in the path of the scattered light.

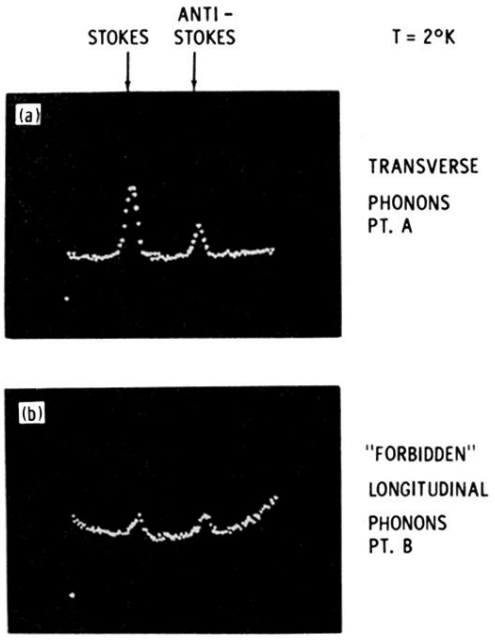

FIG. 14. Same configuration as Fig. 13 except that crystal temperature is now at 2 °K. For integration time used here thermal Brillouin scattering cannot be seen and is below the noise. (a) shows the heating of the transverse phonons upon microwave saturation. The asymmetry in heating of Stokes and anti-Stokes is discussed in text. (b) shows heating of the longitudinal phonons at same frequency to which the spins do not directly couple. Observed heating is ascribed to mode conversion from other heated phonons which couple to the spins.

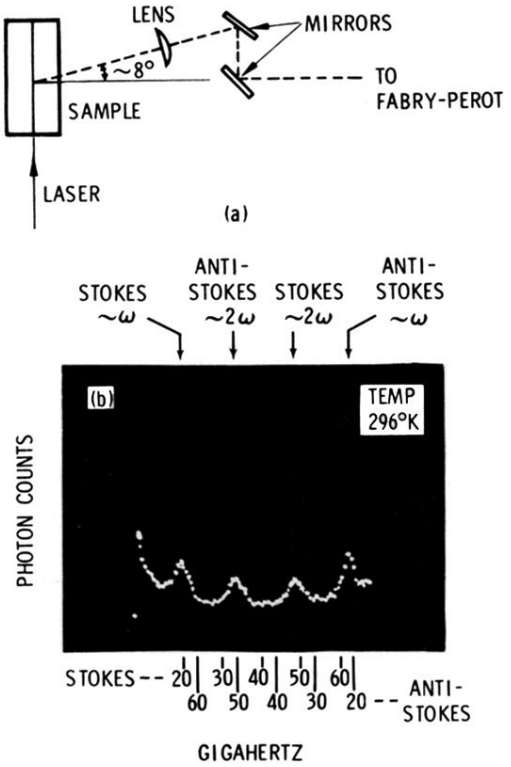

FIG. 16. Thermal Brillouin scattering at room temperature from low-velocity transverse and longitudinal phonons in MgO:Ni^{2+} at frequencies ν and 2ν, respectively. (a) Modification of the 90° scattering geometry of Fig. 3 to view phonons propagating along the [110] crystal direction. Inclusion of the mirrors allows monitoring of these phonons without changing sample orientation or interferometer position. (b) Room-temperature Brillouin spectrum of the low-velocity transverse ($\sim\omega$) and longitudinal ($\sim 2\omega$) phonons using the configuration of (a). Incident laser beam is normal to the dielectric mirror deposited on the sample. Upper and lower frequency scales refer to Stokes and anti-Stokes lines, respectively.

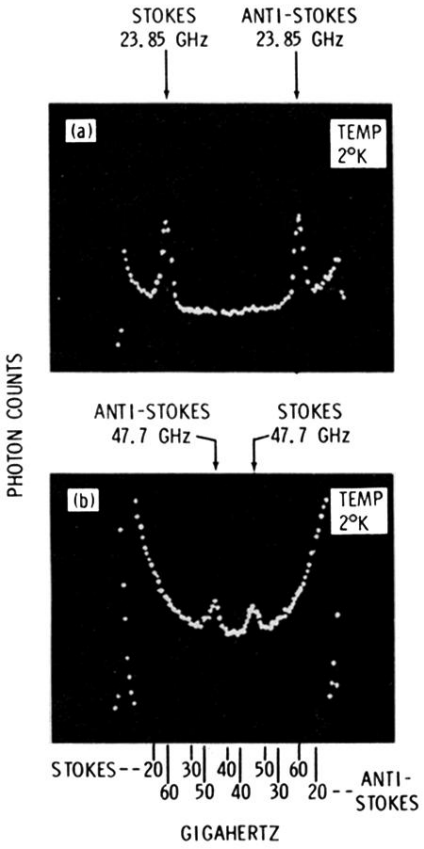

FIG. 17. Brillouin scattering from heated transverse and longitudinal phonons in MgO:Ni^{2+} at a bath temperature of 2 °K. Microwave saturation of the Ni^{2+} spin transitions occurs at 23.85 GHz in an applied field of ~7700 G. (a) Scattering from heated low-velocity transverse phonons at 23.85 GHz. (b) Scattering from heated longitudinal phonons at 47.7 GHz. The spectra of (a) and (b) were obtained with different input-laser-beam orientations, but fixed collection optics; the narrow bandwidths of the heated phonons account for the inability to see both heated phonons in the same spectrum (see text).

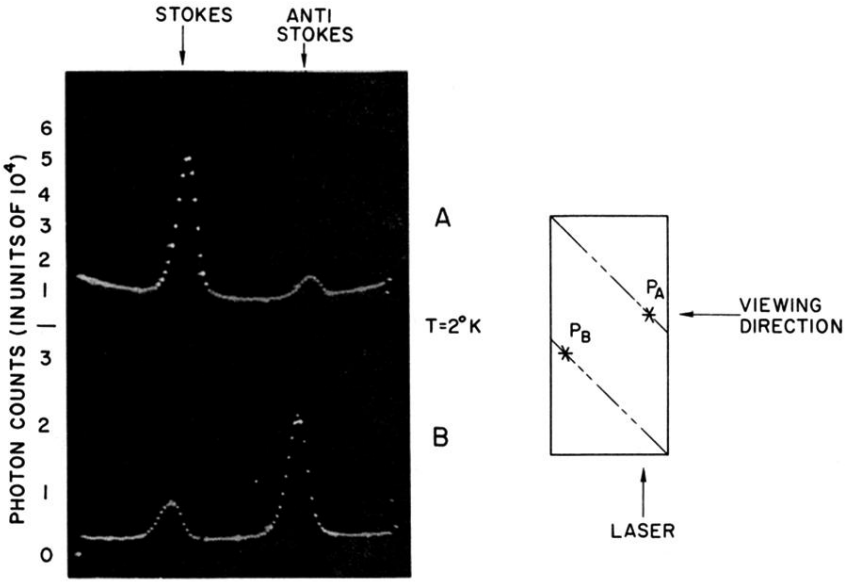

FIG. 19. Brillouin scattering at 2 °K from resonantly heated slow-transverse phonons at 25.6 GHz (labeled $\tilde{q}_A$ in Fig. 4) at points P_A and P_B in planes A and B (shown in Fig. 18), respectively, in sample MS-4A. Note the large asymmetry between Stokes and anti-Stokes phonons and reversal of this asymmetry from A to B. The gain in B has been increased by a factor of 2. The degree of heating shown for the anti-Stokes in A and the Stokes in B roughly corresponds to that described earlier for MS-4A in other regions of the crystal outside these planes. In contrast, the heating of the Stokes in A is anomalously high, i.e., an order of magnitude larger.

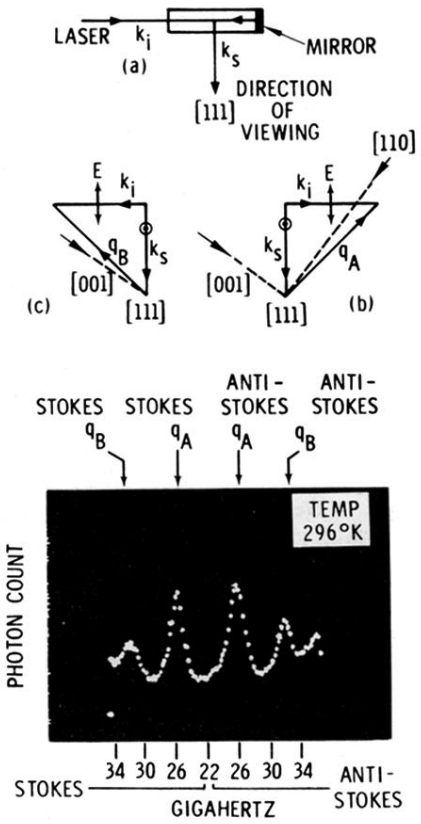

FIG. 4. 90° Brillouin–light-scattering arrangement for MgO:Ni^{2+} crystals. (a) Incident and reflected laser beams are directed along $\pm\vec{k}_i$; the scattered light $\vec{k}_s$ is viewed along the [111] crystal direction. The scattering plane is the $(1\bar{1}0)$ crystal plane. (b) Scattering diagram for incident beam with polarization $\vec{E}$ in the scattering plane; scattered beam polarized normal to scattering plane. Scattering arises from acoustic phonons with wave vector $\pm\vec{q}_A$; dashed lines denote principal axes of the crystal. (c) Scattering diagram for the reflected laser beam; scattering arises from acoustic modes of wave vector $\pm q_B$. Photograph: Room-temperature (296 °K) Brillouin scattering from low-velocity transverse acoustic phonons of wave vector $\vec{q}_A$ and $\vec{q}_B$ in MgO:Ni^{2+}. Abscissa denotes frequency shift of the Stokes and anti-Stokes lines from the laser frequency. Elastic scattering occurs at zero-frequency shift and is not shown.

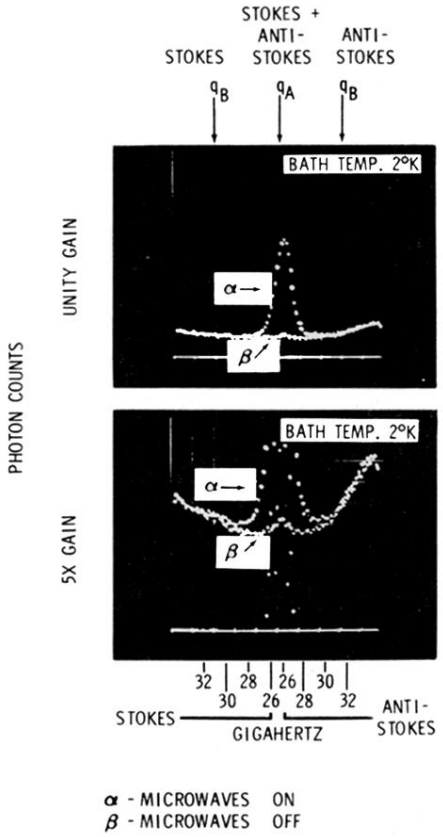

FIG. 5. Brillouin scattering from low-velocity transverse acoustic phonons in MgO:Ni^{2+} at a bath temperature of 2 °K. A magnetic field of 8300 G is applied normal to the $(1\bar{1}0)$ scattering plane. Integration time is 3 min. In order to improve the signal-to-noise ratio, the interferometer spacing has been adjusted so that Stokes and anti-Stokes lines, from adjacent orders, for $\nu(\vec{q}_A)$ shown in Fig. 4 are made to overlap. (α) Microwave saturation of the Ni^{2+} ground-state spin levels at 25.6 GHz, showing a factor-of-30 increase in peak scattering compared to (β). (β) No microwaves, i.e., thermal scattering at 2 °K.

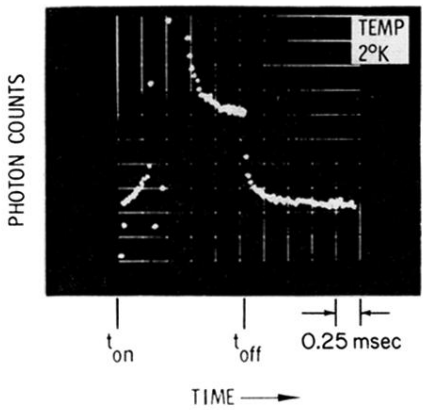

FIG. 8. Relaxation profile for heated low-velocity transverse phonons at a bath temperature of 2 °K. Saturating microwaves are switched on and off at times t_{on} and t_{off}, respectively; each major scale division is 0.25 msec. The rapid variations in phonon heating between t_{on} and t_{off} are due to strong cavity-pulling effects experienced when the spin system is driven from thermal equilibrium at 2 °K to saturation.